

Department of Physics and Astronomy

University of Heidelberg

Master thesis

in Physics

submitted by

Felix Sebastian Herzog

born in Mainz

2022

PENTASIM

A Numerical Simulation of a Penning Trap

This Master thesis has been carried out by

Felix Sebastian Herzog

at the

Max Planck Institute for Nuclear Physics

under the supervision of

Prof. Dr. Klaus Blaum

PENTASIM — A Numerical Simulation of a Penning Trap

Numerical simulations have proven to be an effective approach for studying ion trajectories for different types of mass spectrometers. PENTASIM, developed in this work, is a modular tool for numerical simulation of a single ion in ideal and cylindrical Penning-trap experiments.

The tool uses a polynomial expansion of the electric potentials and magnetic field to allow the calculation of trajectories for different settings that are not constrained by cylindrical symmetry. In particular, realistic maps of the electric potential, e.g. from *Finite Element Method* calculations can be imported. Therefore, PENTASIM is a promising framework for the investigation of systematic effects induced by machining imperfections and higher order terms of the electric potential and magnetic field with the goal of enhancing the sensitivity of state-of-the-art mass spectrometry experiments such as PENTATRAP. In addition, the option to incorporate high-frequency excitation and conversion pulses of any form in the simulation could be leveraged to probe new measurement techniques. The accuracy of the simulation predictions were benchmarked against established theory. Relative residuals below 10^{-8} and 10^{-13} were obtained using a simulation time step of 10^{-12} s for the fast modified cyclotron frequency and slow magnetron frequency, respectively.

PENTASIM — Eine Numerische Simulation einer Penningfalle

Numerische Simulationen haben sich als effektiver Ansatz zur Untersuchung von Ionen-trajektorien für verschiedene Arten von Massenspektrometern erwiesen. PENTASIM, das in dieser Arbeit entwickelt wurde, ist ein modulares Werkzeug für die numerische Simulation eines einzelnen Ions in idealen und zylindrischen Penning-Fallen-Experimenten. Das Tool verwendet eine polynomische Expansion der elektrischen Potentiale und des Magnetfelds, um die Berechnung von Trajektorien für verschiedene Einstellungen zu ermöglichen, die nicht durch zylindrische Symmetrie eingeschränkt sind. Insbesondere können realistische Abbildungen des elektrischen Potentials, z.B. aus *Finite Element Method*-Berechnungen, importiert werden. Daher ist PENTASIM eine vielversprechende Plattform für die Untersuchung von systematischen Effekten, die durch Fertigungsintoleranzen und Terme höherer Ordnung des elektrischen Potentials und des Magnetfelds verursacht werden, mit dem Ziel, die Empfindlichkeit modernster massenspektroskopischer Experimente wie PENTATRAP zu verbessern. Darüber hinaus könnte die Möglichkeit, Hochfrequenzanregungs- und -umwandlungspulse in beliebiger Form in die Simulation einzubeziehen, genutzt werden, um neue Messtechniken zu erproben.

Die Genauigkeit der Simulationsergebnisse wurde mit den theoretischen Vorhersagen abgeglichen. Relative Abweichungen unter 10^{-8} und 10^{-13} wurden mit einem Simulationszeitschritt von 10^{-12} s für die schnelle modifizierte Zyklotronfrequenz bzw. die langsame Magnetronfrequenz erzielt.

Contents

1	Introduction	1
2	Theoretical Background	3
2.1	Penning-Trap Theory	3
2.1.1	Ideal Penning Trap	4
2.1.2	Systematics of the Real Penning Trap	6
2.1.3	Manipulation of the Charged Particle's Motion	9
2.1.4	Analytical Model of a Cylindrical Penning Trap	11
2.2	Simulation Theory	13
2.2.1	Finite Element Method	13
2.2.2	Trilinear Interpolation	14
2.2.3	Regression Analysis	15
2.2.4	Numerical Integration Methods	16
3	Materials, Methods, and Results	19
3.1	Finite Element Method Calculations	20
3.1.1	Numerical Model	20
3.1.2	Integrity of the Electric Potential Calculations	22
3.2	PENTASIM	26
3.2.1	Structure	27
3.2.2	Runtime	29
3.2.3	Minimal Working Examples	29
3.3	Benchmarking	29
3.3.1	Ion Motion	30
3.3.2	Eigenfrequencies	30
3.3.3	Electro-Magnetic Frequency Shifts	32
3.3.4	Excitation and Conversion Pulses	34
4	Discussion	37
5	Conclusion and Outlook	41

Appendix	i
References	v
Acknowledgments	xiii
Declaration	xv

List of Figures

2.1	Hyperbolic and cylindrical Penning trap setup	4
2.2	Trajectory of the harmonic eigenmotions in an ideal Penning trap	6
2.3	Cut through a 5-pole cylindrical Penning trap setup	7
2.4	Sketch of exemplary electrodes used for applying dipole and quadrupole excitation and conversion pulses	10
2.5	Configuration and inverted electric potential of the analytical model of a cylindrical Penning trap	11
2.6	Flow chart of the Finite Element Method (FEM)	13
2.7	Sketch of the trilinear interpolation algorithm	14
3.1	Static electric potential map of the FEM simulations	22
3.2	Convergence of the analytically calculated electric potential	23
3.3	Heat maps of the relative residuals of the FEM simulation compared to the analytical solution	24
3.4	Histograms of the residuals of the interpolation methods compared to the analytical potential for a cubic grid	25
3.5	Histograms of the residuals using the polynomial regression method compared to the analytical potential for a free tetrahedral grid	26
3.6	Flow chart of the PENTASIM simulation package	27
3.7	Temporally recorded spatial data of the ion's motion in the simulation	31
3.8	Residuals of the determined eigenfrequencies as a function of the simulation time step	32
3.9	Electrically induced relative frequency shifts compared to the theoretical expectation	33
3.10	Magnetically induced relative frequency shifts compared to the theoretical expectation	34
3.11	In-phase and opposite-of-phase dipole excitation scheme using an ideal electric potential	35
3.12	Quadrupole conversion scheme using an ideal electric potential	36
3.13	In-phase and opposite-of-phase dipole excitation scheme using an FEM-generated electric potential	36

Chapter 1

Introduction

The mass of an atom serves as a unique fingerprint for identification, providing insight into the atom's state and into the binding energies of its constituents [1]. Over decades of scientific discovery, mass spectrometry has been proven as indispensable for a wide range of research fields not only in physics, but also in chemistry, biology and other basic and applied sciences, where appropriate instruments and methods are successfully being developed [2]. As the frequency is the most precisely measurable quantity to date, reaching relative uncertainties on the order of 10^{-18} [3], it is of no surprise that modern high-precision mass spectrometry is conducted by measurement of the oscillation frequency with which an ion revolves in a magnetic field [1]. The state-of-the-art apparatus for this mass measurement is the Penning trap, which enables the confinement of an ion of interest and offers relative mass uncertainties below 10^{-11} for stable ion species [4].

To study ion trajectories and optimize geometries of various types of mass spectrometers, numerical simulations have been shown to be an effective approach [5]. These include quadrupole ion traps [6], toroidal ion traps [7], Penning ion traps [8–11], sector instruments [12], time-of-flight mass spectrometers [13], Paul ion traps [14], and ion cyclotron resonance instruments [15, 16]. These simulations range from initial calculations for ideal quadrupole fields without resonance and collisions [17] to the inclusion of nonlinear fields [18], collisions with a buffer gas [19], space charge effects [20], image charge shifts [21, 22], sympathetic cooling schemes [23], electrostatic interactions [24, 25], and resonant excitations [26, 27].

The simulation package PENTASIM, which was developed during this work, joins this list by enabling the prediction of ion trajectories in electric potentials deviating from cylindrical symmetry in Penning traps. This provides access to the study of arbitrary shape excitation and conversion pulses, and to systematic effects such as the influence on the charged particle's motion and eigenfrequencies of machining imperfections and higher order terms in the electric potential and magnetic field representations.

Chapter 2

Theoretical Background

This chapter introduces the fundamental concepts required for the remainder of this thesis.

In Sec. 2.1, physical processes of a charged particle inside an ideal and real Penning trap, manipulations to its motion using time-varying electric dipolar and quadrupolar excitation pulses, and a simplified analytical model of a cylindrical trap are described.

In Sec. 2.2, underlying concepts for the simulation studies are laid out which involve the finite element method used for simulating electric potentials, trilinear interpolation and regression analysis for three-dimensional interpolation of an electric potential, as well as numerical integration methods used for propagating a charged particle through an electromagnetic field.

2.1 Penning-Trap Theory

Following Earnshaw's theorem [28], the three-dimensional confinement of a charged particle in a purely static electric potential or purely static magnetic field is impossible. This fact can be explained in simple terms from Gauss's law [29], which states that an electric force $\mathbf{F}(\mathbf{r})$ derived from an electric potential $\phi(\mathbf{r})$ will always be divergence free and satisfy the Laplace equation, resulting in a potential where no local minima nor maxima and only saddle points exist [30].

One of the many solutions to this problem is the so-called Penning-trap solution, where by using a superposition of a static, strong, and uniform magnetic field and a static three-dimensional quadrupole electric potential, charged particles are confined to an equilibrium both radially and axially, respectively [1].

In this section, the concepts of an ideal Penning trap are highlighted as well as the systematic effects which arise in a real trap.

2.1.1 Ideal Penning Trap

In an ideal Penning trap, a charged particle is confined by the superposition of a static, strong, and homogeneous magnetic field aligned along the trap axis for radial confinement and a weak electric quadrupole potential for axial confinement [31]. An illustration and description of the electrodes of a hyperbolic and a cylindrical Penning trap is provided in Fig. 2.1.

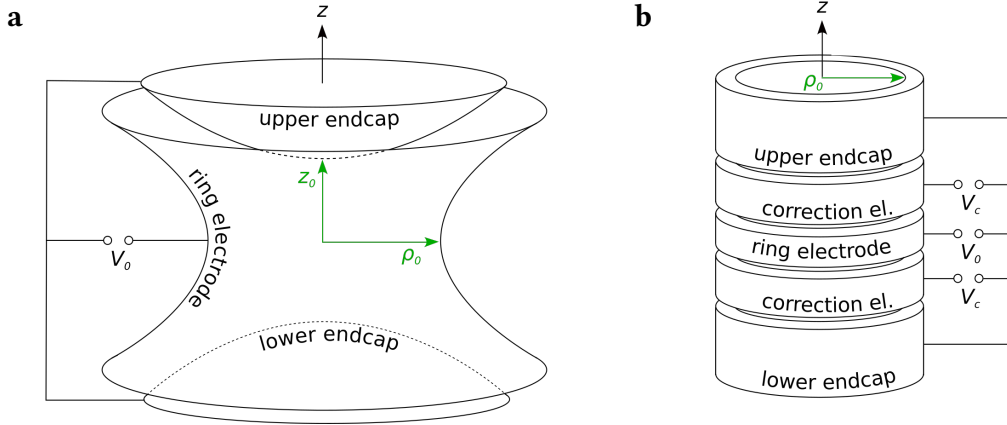


Figure 2.1: Hyperbolic and cylindrical Penning trap setup. In both figures, the voltage V_0 describes the electric potential difference between ring electrode (RE) and end caps (ECs). **(a)** Hyperbolic setup using a hyperbolically shaped RE defined by the radius ρ_0 from the center to the nearest point of the RE, as well as two parabolically shaped ECs defined by the length z_0 from the center to the nearest point of the EC. **(b)** Cylindrical setup using cylindrically shaped electrodes defined by the radius ρ_0 from the center axis of the trap to the nearest point of the respecting electrode in the radial plane. In addition to the potential difference V_0 between the RE and the ECs, a correction voltage V_c is applied between the correction electrodes (CEs) and ECs. Taken and modified from Ref. [32].

The axial magnetic field in z -direction $\mathbf{B} = B_0 \hat{e}_z$ exerts a Lorentz force $\mathbf{F} = q(\mathbf{v} \times \mathbf{B})$ on the ion with charge q , mass m and velocity \mathbf{v} . The resulting angular frequency describing this motion is called the *free cyclotron frequency* ω_c given by

$$\omega_c = \frac{q}{m} B. \quad (2.1)$$

In order to harmonically confine the charged particle in axial direction along the magnetic field lines, an electrostatic quadrupole potential ϕ of the form

$$\phi(\rho, z) = U_0 C_2 \left(z^2 - \frac{\rho^2}{2} \right) \quad (2.2)$$

is imposed, resulting in the electric field \mathbf{E}

$$\mathbf{E}(\mathbf{x}) = -\nabla \phi(\mathbf{x}) = U_0 C_2 (x \hat{e}_x + y \hat{e}_y - 2z \hat{e}_z), \quad (2.3)$$

given in cartesian coordinates $\mathbf{x} \equiv (x, y, z)^\top$. Hereby, the voltage difference U_0 between ring electrode (RE) and end caps (EC) (cf. Fig. 2.1), as well as the geometry dependent harmonic electric potential coefficient C_2 are introduced. In the combined electromagnetic field, the charged particle will experience a total Lorentz force $\mathbf{F} = q(\mathbf{E} + \mathbf{v} \times \mathbf{B})$, resulting in the Newtonian equations of motion

$$\mathbf{F} = q(\mathbf{E} + \dot{\mathbf{x}} \times \mathbf{B}) = m\ddot{\mathbf{x}}. \quad (2.4)$$

This set of coupled differential equations has been solved in multiple publications (cf. [31, 33–36]), yielding the set of solutions of the charged particle's motion

$$x(t) = \rho_+ \sin(\omega_+ t + \varphi_+) + \rho_- \sin(\omega_- t + \varphi_-) \quad (2.5)$$

$$y(t) = \rho_+ \cos(\omega_+ t + \varphi_+) + \rho_- \cos(\omega_- t + \varphi_-) \quad (2.6)$$

$$z(t) = \rho_z \cos(\omega_z t + \varphi_z) \quad (2.7)$$

with its characteristic eigenfrequencies ω_\pm and ω_z

$$\omega_\pm = \frac{1}{2} \left(\omega_c \pm \sqrt{\omega_c^2 - 2\omega_z^2} \right) \quad (2.8)$$

$$\omega_z = \sqrt{\frac{2qU_0C_2}{m}}. \quad (2.9)$$

Here, $\rho_-, \rho_+, \varphi_-, \varphi_+$ describe the radii and the phases of the respective motions in the radial plane, and ρ_z, φ_z in the axial plane, all of which are defined by the initial conditions [33]. The eigenfrequencies ω_-, ω_+ , and ω_z are called the *magnetron frequency*, the *modified cyclotron frequency*, and the *axial frequency*, respectively. An illustration of the three independent motions (in order: green, red, blue) and the combined motion (black) of a charged particle in an ideal Penning trap is visualized in Fig. 2.2. From Eqs. (2.5) and (2.6), and the fact that observable frequencies must not have an imaginary part, it follows that

$$\frac{\omega_c}{\sqrt{2}} > \omega_z \quad (2.10)$$

as a stability condition for trapping [37]. Furthermore, the *free space cyclotron frequency* ω_c is related to the discussed frequencies as

$$\omega_c = \omega_+ + \omega_- \quad (2.11)$$

or analogously

$$\omega_c^2 = \omega_+^2 + \omega_-^2 + \omega_z^2, \quad (2.12)$$

with the latter of the equations being referred to as *Brown-Gabrielse's invariance theorem* [31]. Therefore, by measuring the characteristic eigenfrequencies of a charged

particle in a Penning trap, its mass m can be determined through usage of Eq. (2.1). The hierarchy of the frequencies in terms of their magnitude [21] is expressed by

$$\omega_- \ll \omega_z \ll \omega_+. \quad (2.13)$$

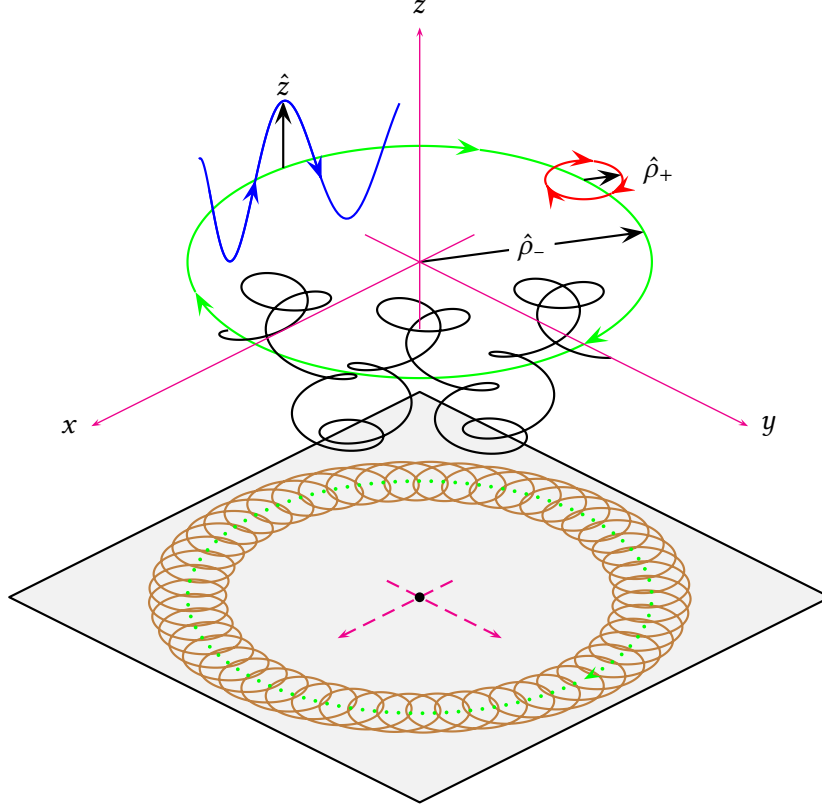


Figure 2.2: Trajectory of the three independent, harmonic eigenmotions of a charged particle in an ideal Penning trap. The blue trajectory describes the axial motion with amplitude \hat{z} , the red trajectory the modified cyclotron motion with amplitude $\hat{\rho}_+$, the green trajectory the magnetron motion with amplitude $\hat{\rho}_-$, and the black trajectory the superposition of all three eigenmotions to a combined motion. The projection onto the xy -plane is shown in brown and dashed green. Taken from Ref. [38].

2.1.2 Systematics of the Real Penning Trap

Unfortunately, the two introduced types of Penning traps described in Sec. 2.1 and Fig. 2.1 cannot be translated into real experimental setups without the introduction of systematic errors along the way for various reasons, such as machining imperfections, the finite lengths of real trap electrodes, and holes in the electrodes for the injection and ejection of charged particles [36].

On the one hand, the mere geometry of a cylindrical trap adds higher order terms to the electric potential compared to a hyperbolic trap. Nevertheless, a nearly perfect

quadrupole electric potential around the center in a confined volume of space can be achieved with cylindrical traps [39]. On the other hand, compared to hyperbolic traps, cylindrical traps provide inherent axial access to the center of the trap, which facilitates ion loading and mixing.

The motivation of calculating systematic errors lies in the charged particle's high sensitivity to a vast number of experimental parameters [40]. In this section, leading systematic effects concerning the electric potential and the magnetic field are discussed for a cylindrical trap geometry, cf. Fig. 2.3.

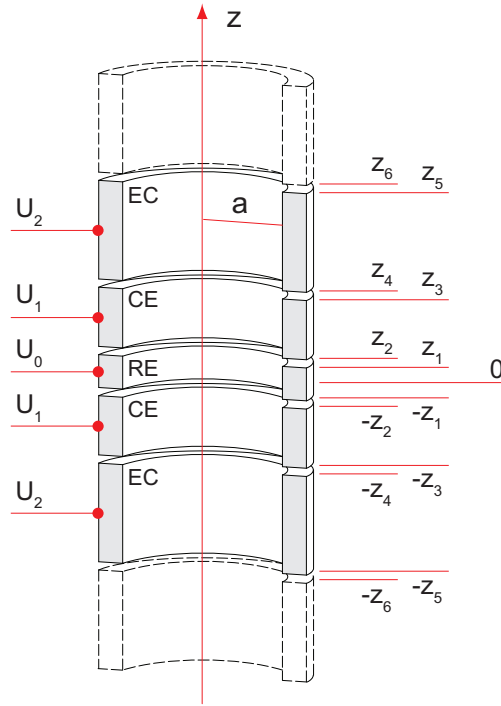


Figure 2.3: Cut through a 5-pole cylindrical Penning trap setup consisting of five electrodes, namely ring electrode (RE), correction electrodes (CEs), as well as the end caps (ECs). The inner radius a from the trap center to the nearest electrode in the radial plane, the electrode voltages U_i , as well as the lengths of the electrodes and the gap lengths between the electrodes $z_j - z_k$ define the trap. Taken from Ref. [36].

Electric Anharmonicities

In the following, all necessary equations for this work were derived in Refs. [36, 41, 42]. The electric potential in a cylindrical Penning trap can be expressed through a Taylor expansion around the center point of the trap. The electric potential ϕ solving *Laplace's equation* $\Delta\phi = 0$, where $\Delta \equiv \nabla^2$ is the *Laplace operator*, can be expressed as

$$\phi(\rho, z) = U_0 \sum_{j=0}^{\infty} \sum_{i=0}^j C_{i,j-i} \cdot \rho^i z^{j-i}, \quad (2.14)$$

with the Taylor coefficients

$$C_{i,j-i} = (-1)^{i/2} \cdot \frac{j!}{(j-i)! \left(\frac{i!}{2}\right)^2 2^i} \cdot C_j, \quad (2.15)$$

and the purely axial coefficients

$$C_j \equiv C_{0,j} = \frac{1}{U_0} \cdot \frac{1}{j!} \cdot \frac{\partial^j \phi(\rho, z)}{\partial z^j} \Big|_{(\rho=0, z=0)}. \quad (2.16)$$

Note that the electric potential is independent of the variable φ due to the inherent rotational symmetry in a cylindrical trap. Hereby, U_0 is the potential difference between the RE and the ECs. Expanding Eq. (2.14) and inserting Eq. (2.15) and Eq. (2.16), the electric potential normalized onto the trapping voltage U_0 can be written as

$$\begin{aligned} \frac{\phi(\rho, z)}{U_0} &= C_0 \\ &+ C_2 \left(z^2 - \frac{1}{2} \rho^2 \right) \\ &+ C_4 \left(z^4 - 3z^2 \rho^2 + \frac{3}{8} \rho^4 \right) \\ &+ C_6 \left(z^6 - \frac{15}{2} z^4 \rho^2 + \frac{45}{8} z^2 \rho^4 - \frac{5}{16} \rho^6 \right) \\ &+ \dots \end{aligned} \quad (2.17)$$

Note, that the odd coefficients are absent since they are suppressed due to the axial symmetry of the electrodes along the z -axis. All relevant frequency-shifts for this thesis, calculated by Ref. [43] and modified to match the definitions in this thesis, i.e. by setting $2d^2 \stackrel{\text{def.}}{=} 1$, are given by

$$\frac{\Delta\omega_z}{\omega_z} = +\frac{3}{4} \frac{C_4}{C_2} \left(\hat{z}^2 - 2\hat{\rho}_+^2 - 2\hat{\rho}_-^2 \right) \quad (2.18)$$

$$\Delta\omega_{\pm} = \mp \frac{3}{2} \frac{C_4}{C_2} \frac{\omega_+ \omega_-}{\omega_+ - \omega_-} \left(2\hat{z}^2 - \hat{\rho}_{\pm}^2 - 2\hat{\rho}_{\mp}^2 \right). \quad (2.19)$$

Magnetic Inhomogeneities

Analog to the discussion of the electric potential, the magnetic field can also be expanded into a *Taylor Series* satisfying *Maxwell's equations*. The second order term [36] is given by

$$\mathbf{B}(\boldsymbol{\rho}, z) = B_0 \hat{\mathbf{e}}_z + B_1 (-2z \hat{\mathbf{e}}_z + \rho \hat{\mathbf{e}}_\rho) + B_2 \left[\left(z^2 - \frac{\rho^2}{2} \right) \hat{\mathbf{e}}_z - z\rho \hat{\mathbf{e}}_\rho \right], \quad (2.20)$$

with the unit vectors $\hat{\mathbf{e}}_\rho$ and $\hat{\mathbf{e}}_z$ in radial and axial direction, respectively. The resulting frequency shifts compared to the calculation of a perfect homogeneous magnetic field

are calculated [43] to be

$$\frac{\Delta\omega_z}{\omega_z} = +\frac{B_2}{4B_0} \frac{\omega_+ + \omega_-}{\omega_+\omega_-} (\hat{\rho}_-^2\omega_- + \hat{\rho}_+^2\omega_+) \quad (2.21)$$

$$\frac{\Delta\omega_+}{\omega_+} = +\frac{B_2}{2B_0} \frac{\omega_+ + \omega_-}{\omega_+ - \omega_-} \left[\hat{z}^2 - \hat{\rho}_+^2 - \hat{\rho}_-^2 \left(1 + \frac{\omega_-}{\omega_+} \right) \right] \quad (2.22)$$

$$\frac{\Delta\omega_-}{\omega_-} = -\frac{B_2}{2B_0} \frac{\omega_+ + \omega_-}{\omega_+ - \omega_-} \left[\hat{z}^2 - \hat{\rho}_+^2 \left(1 + \frac{\omega_+}{\omega_-} \right) - \hat{\rho}_-^2 \right]. \quad (2.23)$$

Further systematic effects such as voltage fluctuations of the power source supplying the electrodes, relativistic shifts due to the charged particle's relative motion to the laboratory coordinate system and its therefore increased inertia, as well as image-charge effects resulting from the charged particle's polarization of the electrodes are discussed in detail e.g. in Ref. [36].

2.1.3 Manipulation of the Charged Particle's Motion

During operation, a charged particle's motion in a Penning trap can be manipulated by superimposing additional electric potentials, frequently exploited using dipolar radio frequency (RF) as well as quadrupolar RF pulses [44]. Concerning the motional modes, a dipolar time-varying excitation with a frequency near the magnetron, modified cyclotron, and axial frequency is used to increase the charged particle's magnetron, modified cyclotron radius or axial amplitude, respectively [45]. Using quadrupolar and octupolar RF fields, a coupling between different modes can be achieved, converting e.g. magnetron motion into cyclotron motion and vice versa [46, 47]. In the following, dipolar and quadrupolar excitations typical to Penning-trap experiments [44] are described following the derivations and reasoning of Ref. [36]. An illustration of example configurations for dipole and quadrupole pulses can be found in Fig. 2.4.

Dipolar Excitation

With a dipolar excitation it is possible to control individual modes of a charged particle inside the trap [45]. By applying time-varying voltages on suitable electrodes of the trap, the superimposed dipole potential $\phi_i^{(d)}$ can be expressed as

$$\phi_i^{(d)}(t) = \phi_{i,0}^{(d)} \cos(\omega_{\text{rf}} t + \varphi_d) \cdot x_i, \quad (2.24)$$

with $i \in \{1, 2, 3\}$ for all three cartesian coordinates and $\phi_{i,0}^{(d)} \equiv \phi_i^{(d)}(t = 0)$, resulting in the componentwise electric field $E_i^{(d)}$

$$E_i^{(d)}(t) = -\nabla\phi_i^{(d)}(t) = -E_{i,0}^{(d)} \cos(\omega_{\text{rf}} t + \varphi_d) \cdot \hat{\mathbf{e}}_i. \quad (2.25)$$

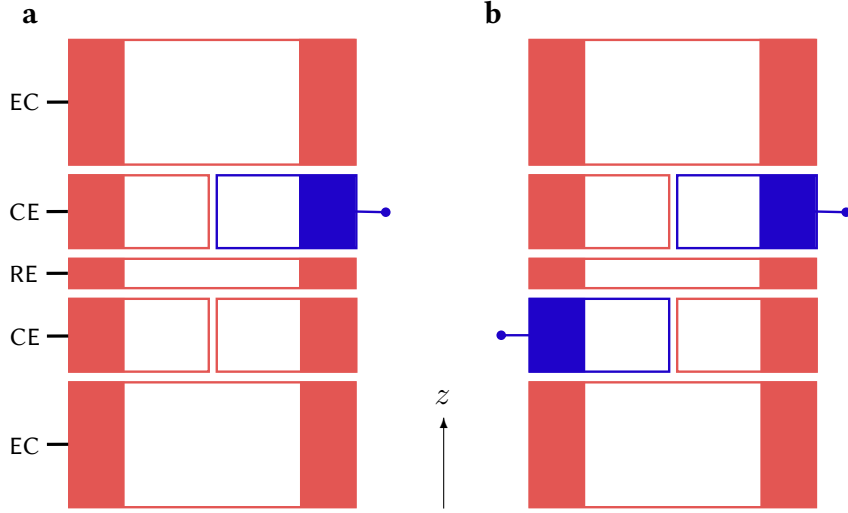


Figure 2.4: Sketch of exemplary electrode configurations used for applying dipole and quadrupole excitation pulses in a cylindrical Penning trap setup consisting of five electrodes named ring electrode (RE), correction electrodes (CEs), and end caps (ECs). All half electrodes operating at a constant potential are depicted in red, whereas all half electrodes superimposed with a time-varying RF potential in addition to their respective constant potentials are depicted in blue. **(a)** Example configuration of a dipole pulse using half of the upper-right CE for applying the time-varying potential. **(b)** Example configuration of a quadrupole pulse using half of the upper-right CE and half of the lower-right CE for applying the time-varying potential. Taken and modified from Ref. [40].

Assuming the electric field \mathbf{E} to be directed in positive x -direction and introducing the acceleration $a_0 \equiv qE_0^{(d)}/m$, the time-dependent modified cyclotron and magnetron radii $\rho_+(t)$, $\rho_-(t)$ are given by

$$\rho_{\pm}(t) = \sqrt{\rho_{\pm}^2(0) + \frac{a_0^2}{4(\omega_+ - \omega_-)^2} \cdot t^2} \mp \frac{\rho_{\pm} a_0 \sin[\varphi_d - \varphi_{\pm}(0)]}{\omega_+ - \omega_-} \cdot t. \quad (2.26)$$

Quadrupolar Excitation

Using a quadrupolar excitation pulse, two eigenmotions can be converted into one another [36]. The coupling of the two radial modes has been considered in Ref. [47], whereas the coupling of the axial to both radial modes has been covered in Ref. [48]. A quadrupolar electric coupling field is of the form

$$\mathbf{E}_{i,j}^{(q)}(t) = E_0^{(q)} \cos(\omega_{\text{rf}} t + \varphi_q) (x_j \hat{\mathbf{e}}_i + x_i \hat{\mathbf{e}}_j). \quad (2.27)$$

Complying with the resonance condition $\omega_{\text{rf}} = \omega_- + \omega_+$ for converting two radial modes into one another, the time evolution can be written as

$$\rho_{\pm}(t) = \rho_{\pm}(0) \cos\left(\frac{\Omega_0}{2} \cdot t\right) \mp \rho_{\mp}(0) \sin\left(\frac{\Omega_0}{2} \cdot t\right) \cos(\varphi_q - \varphi_+ - \varphi_-), \quad (2.28)$$

with the *Rabi frequency* Ω_0 given by

$$\Omega_0 = \frac{q}{m} \cdot \frac{E_0^{(q)}}{2(\omega_+ - \omega_-)}, \quad (2.29)$$

defining the beating frequency $\Omega_0/2$ between the two radial modes and the conversion time $T_c = \pi/\Omega_0$.

In addition, the Rabi frequency for the coupling of the axial mode to one of the radial modes Ω_0^{ax} is given by [48]

$$\Omega_0^{\text{ax}} = \frac{q}{m} \cdot \frac{E_0^{(q)}}{2\sqrt{\omega_z(\omega_+ - \omega_-)}}. \quad (2.30)$$

2.1.4 Analytical Model of a Cylindrical Penning Trap

Analytically modeling a cylindrical Penning trap can be achieved by defining a set of prerequisites and by exploiting the cylindrical and mirror symmetry in the system. In Fig. 2.5 the configuration of a stack of three adjacent traps is shown on the top as well as the negative potential through the center axis z of the trap, expanding to half of the total trap length L in negative as well as in positive z -axis. It is important to note that the number of traps in the configuration was arbitrarily chosen to be three, whereas the following derivation is valid for any odd number of traps.

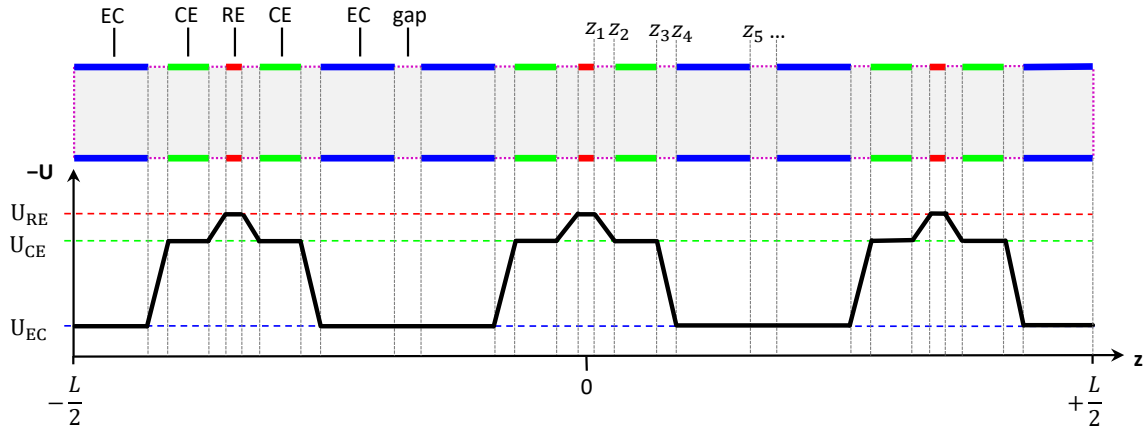


Figure 2.5: Configuration (top) and resulting inverted electric potential (bottom) of a stack of three adjacent Penning traps as a section along the center axis z . The electrodes are grouped by color according to their type, where the ring electrodes (REs) are depicted in red, the correction electrodes (CEs) in green, and the end caps (ECs) in blue. Fictional gap potentials (dashed purple) between the electrodes are introduced, linearly interpolating the potential between two adjacent electrodes, defining a complete set of boundary conditions necessary for calculating the inner potential using *Laplace's equation*. Furthermore, the points z_j with $j \in \{0, 1, \dots, m\}$, with the total number of electrodes m , are defined as the start (end) points of the electrodes in only the positive half space, assuming mirror symmetry at $z = 0$.

The following derivation follows along the textbook solution found in Ref. [49], where radial symmetry perpendicular to the z -axis as well as mirror symmetry on the plane with $z = 0$ is assumed.

Laplace's equation in cylindrical coordinates is given by

$$\Delta\phi \equiv \nabla^2\phi = \frac{1}{\rho} \frac{\partial}{\partial\rho} \left(\rho \frac{\partial\phi}{\partial\rho} + \frac{\partial^2\phi}{\partial z^2} \right) = 0. \quad (2.31)$$

Here, the separation ansatz $\phi(\rho, z) = R(\rho) Z(z)$ can be used to split radial and axial part, yielding the general solution

$$\Delta\phi(\rho, z) = \int_{-\infty}^{+\infty} dk R(k\rho) Z(kz), \quad (2.32)$$

with

$$R(k\rho) = C(k) I_0(k\rho) \quad (2.33)$$

$$Z(kz) = A(k) \cos(kz), \quad (2.34)$$

thereby leaving the electric potential to be calculated by the integral

$$\phi(\rho, z) = \int_{-\infty}^{+\infty} dk A(k) C(k) I_0(k\rho) \cos(kz). \quad (2.35)$$

Here, the coefficients $A(k)$ are defined by the *Dirichlet boundaries*, namely the geometry of the electrode as well as its corresponding electric potential. The solution of the electric potential for a stack of adjacent traps can then be written as

$$\phi(\rho, z) = \lim_{n_{\max} \rightarrow \infty} \frac{4}{L} \sum_{\substack{n=1 \\ n \text{ odd}}}^{n_{\max}} \sum_{i=1}^{(m-1)/2} \frac{U_i - U_{i-1}}{l_{\text{gap}} k_n^2 I_0(k_n a)} \left(\cos(k_n z_{2i}) - \cos(k_n z_{2i-1}) \right) I_0(k_n \rho) \cos(k_n z), \quad (2.36)$$

using the total length L of the trap, the lengths of the gaps between the electrodes l_{gap} , the total number of electrodes m , the electrode potentials U_j , the inner trap radius a , the factor $k_n = n\pi/L$, the *modified Bessel function* of 0th order I_0 , and the enumerated electrode start (end) positions z_j with $j \in \{0, 1, \dots, m\}$, are defined as the start (end) points of the electrodes. It is important to note that these electrode positions enter Eq. (2.36) only in the positive (negative) half space of z , implicitly assuming mirror symmetry at $z = 0$. Furthermore, as also radial symmetry perpendicular to the z -axis located at $x = y = 0$ is also assumed, effects of half electrode voltages (concerning only an angle of π of the respective electrode surface expressed in radians) are not covered. Due to the assumed mirror symmetries it is not possible to mathematically apply the potential of a single electrode U_j on one half electrode without forcibly changing the potential U_j on the

other half electrode. Therefore, the analytical solution provided in Eq. (2.36) cannot be leveraged for studying the application of pulses, except axially, on a charged particle described in Sec. 2.1.3, as this would require a mirror-symmetry breaking consideration of the electric potential.

2.2 Simulation Theory

This section describes the theoretical tools used in the simulation, namely the finite element method for numerically calculating the electric potentials, trilinear interpolation and regression analysis for interpolation between grid points, and the numerical integration methods used to displace a charged particle through an electromagnetic field.

2.2.1 Finite Element Method

The *Finite Element Method* (FEM) is a frequently proposed method to solve static and (or) dynamic behavior of physical systems in linear or non-linear regions in one-, two- or three-dimensional domains in the form of partial differential equations (PDEs). An FEM calculation requires intensive use of computational resources by using a simple approximation of unknown variables for transforming PDEs into algebraic equations [50].

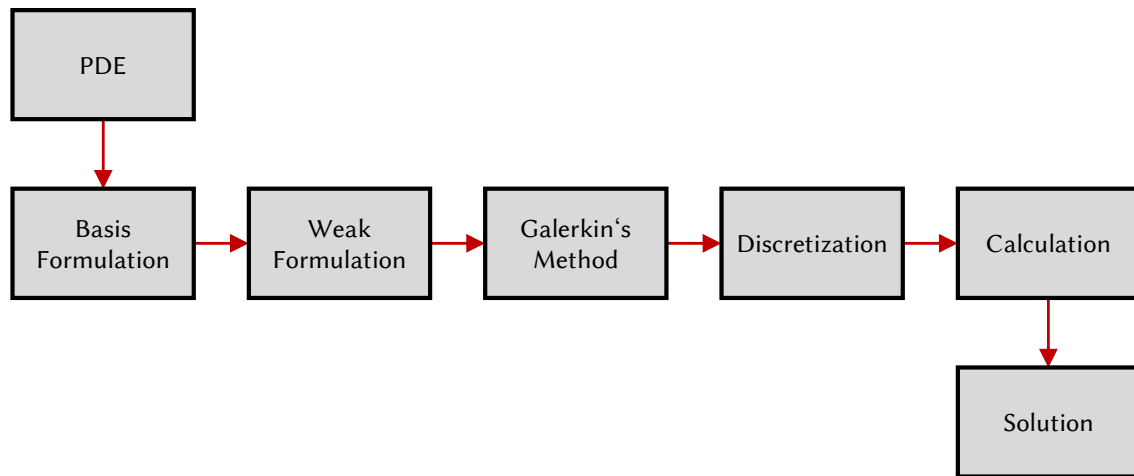


Figure 2.6: Flow chart of the *Finite Element Method* (FEM). Taken and modified from Ref. [22].

The mathematical derivation of the FEM along with its applications has been extensively studied in articles and textbooks [50–53]. Here, only a comprehensive overlook is provided. A coarse sketch of the procedure of the FEM as laid out by Ref. [22] is provided in Fig. 2.6. First, all partial differential equations (PDEs) including all boundary conditions must be established from the task at hand. Second, a basis needs to be defined, serving as an approximation to the true solution. Third, all non-differentiable boundary conditions in the model (e.g. leaps in a parameter) will be smoothed to allow for differentiation.

Fourth, *Galerkin's method* allows updating of the basis using the residuals such that it approaches the true solution. Fifth, the problem is discretized to mesh units, allowing for the set of linear equations to be solved. Finally, we yield the basis representation of the system with updated parameters, which can be used to approximate the true solution.

2.2.2 Trilinear Interpolation

Trilinear interpolation is a method of multivariate interpolation on a three-dimensional regular lattice, i.e. the three-dimensional extension of the two-dimensional bilinear interpolation and the one-dimensional linear interpolation. Using this method, the value of an intermediate point inside a cubic lattice is approximated by finding the smallest cuboid still containing the point. One way to visualize the algorithm is that contributions from all eight corners are used to calculate a linear weighted sum, where the weight is given by the ratio of volume of the cuboid whose diagonal axis is formed by the given point and the diagonally opposite corner to the volume of the cuboid formed by the cell [54].

One algorithm for trilinearly interpolating a given point within a cubic lattice is stated in the following using the notation introduced in Fig. 2.7.

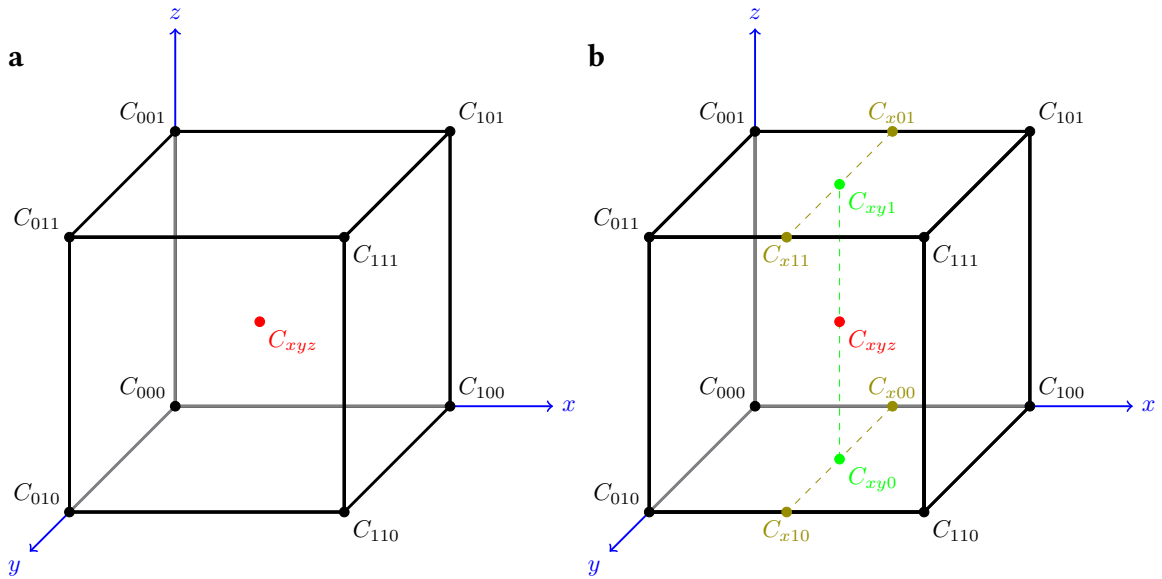


Figure 2.7: Sketch of the trilinear interpolation algorithm: Eight corner points of a cuboid (black) taken from a cubic lattice with arbitrary side lengths in all three cartesian coordinates enclose a point C_{xyz} (red), to which the trilinear interpolation is applied.

Given a point C_{xyz} with coordinates $(\tilde{x}, \tilde{y}, \tilde{z})$ in an arbitrary periodic cubic lattice, one can find eight surrounding points of this lattice to which the function $f(x, y, z)$ is known. These points are enumerated according to C_{ijk} indicated in Fig. 2.7a, where $i, j, k \in \mathbb{N}$ are the grid positions in the respective directions and values c_{ijk} . Now, we can define

and calculate the differences x_d, y_d, z_d using the coordinates x_i, y_j, z_k of the mentioned surrounding grid points as

$$x_d \equiv \frac{\tilde{x} - x_i}{x_{i+1} - x_i} \quad (2.37)$$

$$= \frac{\hat{x} - x_0}{x_1 - x_0}, \quad (2.38)$$

and analogue for y_d and z_d . Finally, we can calculate the function $f(\tilde{x}, \tilde{y}, \tilde{z})$ at point C_{xyz} by performing a composition of three linear interpolations along each axis (cf. Fig. 2.7b), where the order of execution is irrelevant because of their intrinsic linearity. Here, the linear interpolations \mathbb{L} are executed in order of $\mathbb{L} = \mathbb{L}_x \circ \mathbb{L}_y \circ \mathbb{L}_z$. First, interpolating along the x -axis

$$c_{x00} = c_{000} (1 - x_d) + c_{100} x_d \quad (2.39)$$

$$c_{x01} = c_{001} (1 - x_d) + c_{101} x_d \quad (2.40)$$

$$c_{x10} = c_{010} (1 - x_d) + c_{110} x_d \quad (2.41)$$

$$c_{x11} = c_{011} (1 - x_d) + c_{111} x_d, \quad (2.42)$$

then interpolating along the y -axis

$$c_{xy0} = c_{x00} (1 - y_d) + c_{x10} y_d \quad (2.43)$$

$$c_{xy1} = c_{x01} (1 - y_d) + c_{x11} y_d, \quad (2.44)$$

and finally interpolating along the z -axis

$$c_{xyz} = c_{xy0} (1 - z_d) + c_{xy1} z_d. \quad (2.45)$$

Hence, the linearly approximated value in three dimensions at the point C_{xyz} is given by the result $f(\tilde{x}, \tilde{y}, \tilde{z}) \approx c_{xyz}$.

2.2.3 Regression Analysis

Regression analysis seeks to solve problems where the goal is to build a system taking a feature vector $\mathbf{x}_i \in \mathbb{R}^m$ of independent variables as input and predicting the value of an output scalar $y_i \in \mathbb{R}$ as the dependent variables with the help of unknown parameters $\beta \in \mathbb{R}^m$ and error terms $\varepsilon_i \in \mathbb{R}$ for every data point with index $i \in \{1, 2, \dots, n\}$ [55]. The error terms are assumed to follow a normal distribution $\varepsilon_i \sim \mathcal{N}(0, \sigma^2)$, centered around zero with mean $\mu = 0$ and variance σ^2 , and are not directly observable.

In their most general form, regression models are therefore described by

$$y_i = f(\mathbf{x}_i, \boldsymbol{\beta}) + \varepsilon_i, \quad (2.46)$$

where the function $f(\mathbf{x}_i, \boldsymbol{\beta})$ is estimated to closely resemble the data y_i [56]. Once a statistical model has been chosen, the model is fit to the data by minimizing an error function such as e.g. *ordinary least squares* (cf. Ref. [57]), finding estimates $\hat{\boldsymbol{\beta}}$ for the unknown true parameters $\boldsymbol{\beta}$.

Assuming a total of n data points and employing the *ordinary least squares* criterion onto Eq. (2.46) yields

$$r_i(\boldsymbol{\beta}') = y_i - \hat{y}_i = y_i - [f(\mathbf{x}_i, \boldsymbol{\beta}') + \varepsilon_i], \quad (2.47)$$

for the residuals r_i , and therefore the final sum of the squared residuals to be minimized as

$$\hat{\boldsymbol{\beta}} = \min_{\boldsymbol{\beta}'} \sum_{i=1}^n r_i^2(\boldsymbol{\beta}'). \quad (2.48)$$

The general solution [56] to this equation in matrix notation for all n data points is given by

$$\hat{\boldsymbol{\beta}} = (\mathbf{X}^\top \mathbf{X})^{-1} \mathbf{X}^\top \mathbf{y}, \quad (2.49)$$

where $\mathbf{X} \in \mathbb{R}^{n \times m}$ is the so-called design matrix with its transpose $\mathbf{X}^\top \in \mathbb{R}^{m \times n}$, the dependent variables vector $\mathbf{y} \in \mathbb{R}^n$, and the estimator of the unknown parameter vector $\hat{\boldsymbol{\beta}} \in \mathbb{R}^m$.

2.2.4 Numerical Integration Methods

Numerical methods for first-order ordinary differential equations seek to solve initial value problems of the form [58]

$$\frac{d\mathbf{y}}{dt} = \mathbf{f}(t, \mathbf{y}) \quad \text{with} \quad \mathbf{y}(t_0) = \mathbf{y}_0, \quad (2.50)$$

where the function \mathbf{f} is defined as $\mathbf{f} : [t_0, \infty) \times \mathbb{R}^d \rightarrow \mathbb{R}^d$, with the initial time t_0 and the dimension d , and $\mathbf{y}_0 \in \mathbb{R}^d$ defining the initial state vector. For solving these problems, numerous numerical methods exist, which can be coarsely classified into *linear multistep* and *Runge-Kutta* approaches, being either of implicit or explicit type [59].

In this thesis, one particular initial value problem is of great importance, namely the integration of a charged particle in an arbitrary, time-dependent, electromagnetic field. According to the equation of motion of a charged particle in such a field, given by

Eq. (2.4), the derived first-order initial value problem of the form of Eq. (2.50) yields

$$\frac{d\mathbf{x}}{dt} = \mathbf{v} \quad (2.51)$$

$$\frac{d\mathbf{v}}{dt} = \frac{q}{m}(\mathbf{E} + \mathbf{v} \times \mathbf{B}) \quad \text{with} \quad \mathbf{v}(t_0) = \mathbf{v}_0, \quad (2.52)$$

with the position vector \mathbf{x} , the velocity vector \mathbf{v} , the charge q and mass m of the particle, the electric field vector \mathbf{E} , the magnetic field vector \mathbf{B} , as well as the initial velocity \mathbf{v}_0 at time t_0 .

Boris Algorithm

The advancing of a charged particle in an electromagnetic field can e.g. be numerically integrated using *Boris' algorithm* [60–63]. The derivation of the algorithm in the following is strongly based on Refs. [64, 65].

For a given phase space coordinate $(\mathbf{x}_k, \mathbf{v}_k)$ at the k^{th} time step $t_k = k \cdot \Delta t$, the *Boris algorithm* solves for the advanced phase space coordinate of the particle $(\mathbf{x}_{k+1}, \mathbf{v}_{k+1})$ at the $(k+1)^{\text{th}}$ time step $t_{k+1} = (k+1) \cdot \Delta t$, by discretizing the equations of motion Eqs. (2.51) and (2.52)

$$\frac{\mathbf{x}_{k+1} - \mathbf{x}_k}{\Delta t} = \mathbf{v}_{k+1} \quad (2.53)$$

$$\frac{\mathbf{v}_{k+1} - \mathbf{v}_k}{\Delta t} = \frac{q}{m} \left(\mathbf{E}_k + \frac{(\mathbf{v}_{k+1} + \mathbf{v}_k) \times \mathbf{B}_k}{2} \right). \quad (2.54)$$

Here, Δt denotes the time step, and the quantities $\mathbf{x}_k \equiv \mathbf{x}(k)$, $\mathbf{v}_k \equiv \mathbf{v}(t_k - \Delta t/2)$, $t_k \equiv k \cdot \Delta t$, $\mathbf{E}_k \equiv \mathbf{E}(\mathbf{x}_k)$, and $\mathbf{B}_k \equiv \mathbf{B}(\mathbf{x}_k)$ are defined. There exist many equivalent ways of solving Eqs. (2.53) and (2.54) explicitly for the next time step [66]. One of them is to separate the electric and magnetic forces like

$$\mathbf{v}^- = \mathbf{v}_k + \frac{q}{m} \mathbf{E}_k \frac{\Delta t}{2} \quad (2.55)$$

$$\frac{\mathbf{v}^+ - \mathbf{v}^-}{\Delta t} = \frac{q}{2m} (\mathbf{v}^+ + \mathbf{v}^-) \times \mathbf{B}_k \quad (2.56)$$

$$\mathbf{v}^+ = \mathbf{v}_{k+1} - \frac{q}{m} \mathbf{E}_k \frac{\Delta t}{2}, \quad (2.57)$$

and perform the rotations

$$\mathbf{v}' = \mathbf{v}^- + \mathbf{v}^- \times \mathbf{t} \quad (2.58)$$

$$\mathbf{v}^+ = \mathbf{v}^- + \mathbf{v}' \times \mathbf{s} \quad (2.59)$$

with the help of

$$\mathbf{t} \equiv \frac{q}{m} \mathbf{B}_k \frac{\Delta t}{2} \quad (2.60)$$

$$\mathbf{s} = \frac{2\mathbf{t}}{1 + |\mathbf{t}|^2}. \quad (2.61)$$

Now, *Boris' algorithm* is given by the one-step map

$$\Psi_B : \mathbf{z}_k \equiv (\mathbf{x}_k, \mathbf{v}_k) \mapsto \mathbf{z}_{k+1} \equiv (\mathbf{x}_{k+1}, \mathbf{v}_{k+1}), \quad (2.62)$$

consecutively following the subsequent procedure:

1. Calculate the rotation vectors \mathbf{t} and \mathbf{s} , cf. Eqs. (2.60) and (2.61).
2. Calculate \mathbf{v}^- by adding half of the electric impulse, cf. Eq. (2.55).
3. Calculate the bisector velocity \mathbf{v}' , cf. Eq. (2.58).
4. Calculate \mathbf{v}^+ by a rotation of \mathbf{v}^- , cf. Eq. (2.59).
5. Calculate \mathbf{v}_{k+1} by adding half of the electric impulse to \mathbf{v}^+ , cf. Eq. (2.57).

Chapter 3

Materials, Methods, and Results

The goal of this thesis has been to create a simulation package for studying the motion of a charged particle in a Penning trap with arbitrary, cylindrical symmetry breaking electrode geometry. In addition, the package should enable the study of systematic effects as well as of excitation and conversion procedures, i.e. the conversion of the different motional modes into each other. To achieve this goal, several challenges had to be addressed:

1. Developing a procedure for calculating static or dynamic, non-symmetric, electric trap potentials and their superposition for a given electrode geometry.
2. Finding a suitable software base (programming languages, tools, etc.) and an integration algorithm that meets the set requirements.
3. Sufficiently optimizing the simulation to the problem (vectorization, in-place operations, static arrays, etc.) in order to be temporally feasible for scientific usage.
4. Support of parameter studies by built-in access to parallelized computing architecture to minimize overall runtime.
5. Programming an easy-to-use and intuitive interface operated by only a few lines of code.
6. Support of custom, user-defined scripts for simulation that can be written in any programming language.
7. Testing and comparing the simulation results to already published theoretical calculations to benchmark its capabilities and limits.
8. Wrapping everything up into a customizable, maintainable, and extendable software package efficiently running with contemporary, off-the-shelf office computers.

3.1 *Finite Element Method Calculations*

Numerical simulations such as the *Finite Element Method* (FEM, cf. Sec. 2.2.1) provide the opportunity to calculate solutions to problems not yet analytically determined or feasible by solving the problem's underlying partial differential equations (PDEs) with given boundary conditions, yielding an approximation to the true solution.

For this thesis, special emphasis was put on the calculation of static or dynamic electric potentials breaking the cylindrical symmetry for studying machining errors (e.g. offset, tilt of electrodes) and radio frequency (RF) excitation and conversion pulses (cf. Sec. 2.1.3). Fortunately, well-tested commercial programs such as COMSOL¹ and SIMION² can be resorted to, both providing an abundance of FEM solvers. For this work, COMSOL has been chosen over SIMION since the latter program has no capability of adaptive meshing, which concentrates grid elements towards regions in space with large gradients [67], thus increasing computational efficiency without sacrificing accuracy [68].

To analyze the effect of the density of the mesh grid in the COMSOL simulations, the numerical and analytical potentials were compared to one another by calculating relative residuals at numerous points for varying degrees of freedom (DOF). This study resulted in an increase of accuracy of the simulation for increasing DOF, as expected. Therefore, all calculations in this thesis were carried out using the highest number of DOF possible with the available computing infrastructure, summing up to a total of ~109 million.

3.1.1 *Numerical Model*

The numerical model used for the calculation of all half electrode potentials in the trap tower was replicated in COMSOL from the analytical model described in Sec. 2.1.4, serving as a minimal working example and proof-of-principle model. It is important to note that despite having the same setup, the numerical model is able to break the cylindrical symmetry of the electric potential, which is not the case for the analytical model discussed. Therefore, the resulting electric potentials of both models can only be compared for cases when the cylindrical symmetry and the mirror symmetry at $z = 0$ of the boundary conditions is respected.

The number of adjacent traps in the stack was chosen to be three as a trade-off between the computation time of the electric potential and its accuracy. To resemble the experimental setup PENTATRAP at the Max Planck Institute for Nuclear Physics (MPIK) in the scope of this model as closely as possible, the parameters for an orthogonal and compensated Penning trap tower calculated in Ref. [36] were used. Errors in electrode lengths due to thermal shrinkage from room temperature to cryogenic operating temperature are expected to be less than 1 μm [40] and are therefore neglected. Important COMSOL-specific

¹<https://www.comsol.com/>, accessed 2022/02/02

²<https://simion.com/>, accessed 2022/02/02

parameters, which were used for the simulation, are listed in Tab. 3.1. Furthermore, a cylindrical volume was defined in the center of the trap with radius $r_{\text{cyl}} = 100 \mu\text{m}$ and height $h_{\text{cyl}} = 200 \mu\text{m}$, setting the grid size to the lowest extent a_{min} , forcing COMSOL to mesh finely in and close around this self-defined region of interest (ROI). The default minimum and maximum grid element sizes recommended by COMSOL were used and refined empirically to maximize the number of grid points used and therefore increase the accuracy of the simulation to a point where it runs stable on the MPIK cluster without running out of random access memory (RAM). The relative tolerance τ refers to the convergence criterion of the FEM algorithm in COMSOL, i.e.

$$\delta_i = \left| \frac{U_i - U_{i-1}}{U_i} \right| \stackrel{!}{<} \tau \quad (3.1)$$

with the element-wise relative residuals δ_i with electric potential voltage U_i at iteration step i . The relative tolerance threshold of $\tau = 10^{-15}$ was chosen to be equivalent to the resolution of a 64-bit double-precision floating-point representation in PYTHON's NUMPY package [69], being approximately an order of magnitude coarser than one machine epsilon $\varepsilon = 2^{-52} \approx 2 \times 10^{-16}$ of this representation [70]. All other parameters were left to their default values. A depiction of a solution to the described model with the discussed set of boundary conditions (cf. 2.1.4) is visualized in Fig. 3.1.

Table 3.1: Parameter settings used in the COMSOL simulation. The values were calculated in Ref. [36] for an orthogonal and compensated trap tower. The COMSOL-specific grid element sizes a_{min} , a_{max} and the relative tolerance τ were chosen independently of these calculations. The electrode voltages were set to values that would allow them to be easily scaled by a factor at a later stage.

Description	Symbol	Value	Unit
Tuning Ratio	TR	0.881	a.u.
Gap Length	L_{gap}	0.15	mm
RE Length	L_{RE}	1.457	mm
CE Length	L_{CE}	3.932	mm
EC Length	L_{EC}	7.040	mm
Inner Trap Radius	R	5	mm
Single Trap Length	L_{trap}	24.15	mm
RE Voltage	V_{RE}	1	V
CE Voltage	V_{CE}	0.881	V
EC Voltage	V_{EC}	0	V
Min. Grid Element Size	a_{min}	1.45	μm
Max. Grid Element Size	a_{max}	145	μm
Relative Tolerance	τ	10^{-15}	a.u.

From the electrode lengths L_{RE} , L_{CE} , L_{EC} and the gap length L_{gap} given in Tab. 3.1 the electrode positions z_j introduced in Sec. 2.1.4 and visualized in Figs. 2.3 and 2.5 can

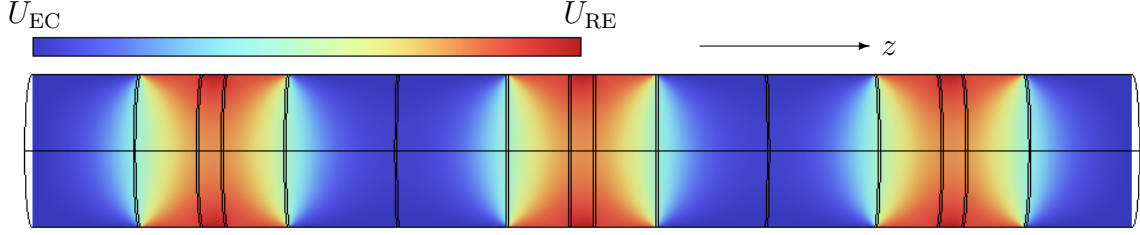


Figure 3.1: Depiction of the numerically calculated, color-coded static electric potential in a slice along the center axis of the Penning-trap tower from the FEM simulation in COMSOL. The colorbar ranges linearly from the end cap voltage U_{EC} in blue to the ring electrode voltage U_{RE} in red, whose values are taken from Tab. 3.1.

be calculated recursively by

$$z_0 \equiv 0 \quad (3.2)$$

$$z_j = z_{j-1} + L_{j-1}, \quad (3.3)$$

with $j \in \{1, \dots, m\}$ and total electrode number m , and the lengths

$$L_0 = \frac{L_{RE}}{2} \quad (3.4)$$

$$L_j = \begin{cases} L_{\text{electrode}} & \text{if } j \text{ even} \\ L_{\text{gap}} & \text{if } j \text{ odd,} \end{cases} \quad (3.5)$$

counting through the electrodes from inside to outside in their order of appearance in the trap tower.

3.1.2 Integrity of the Electric Potential Calculations

To clarify the integrity of the analytical and numerical simulations, a series of calculations were performed. The two goals of these calculations were to ensure the convergence of the analytical implementation, and to compare the interpolated numerical calculations through trilinear interpolation and polynomial regression to the known analytical solution of the electric potential.

Convergence of the Analytical Electric Potential Calculations

The analytical electric potential solution for a stack of ideal cylindrical Penning traps is introduced in Sec. 2.1.4. For proving the convergence of the analytical solution implementation, a number of $N = 100\,000$ points were drawn from a uniform distribution using a fixed highest order n_{max} , up to which the terms of the sum from Eq. (2.36) were calculated. The cube-like region of interest (ROI) was chosen to be in the interval $[-1, +1]$ mm for all three cartesian coordinates with the cube's center being the center of the trap. The

iteration counter i is defined to number consecutively through all orders n_{\max} for a simplified formulation in the following discussion. Then, the relative residuals δ_i from Eq. (3.1) were calculated for each point between each order i and preceding order $i - 1$, from which mean $\bar{\delta}_i$ and standard deviation σ were calculated. The result is visualized in Fig. 3.2. The relative tolerance threshold τ (cf. Tab. 3.1) employed in the COMSOL simulation and discussed in Sec. 3.1.1 is chosen as the minimal accuracy needed for comparing the analytical and numerical potential at a later step.

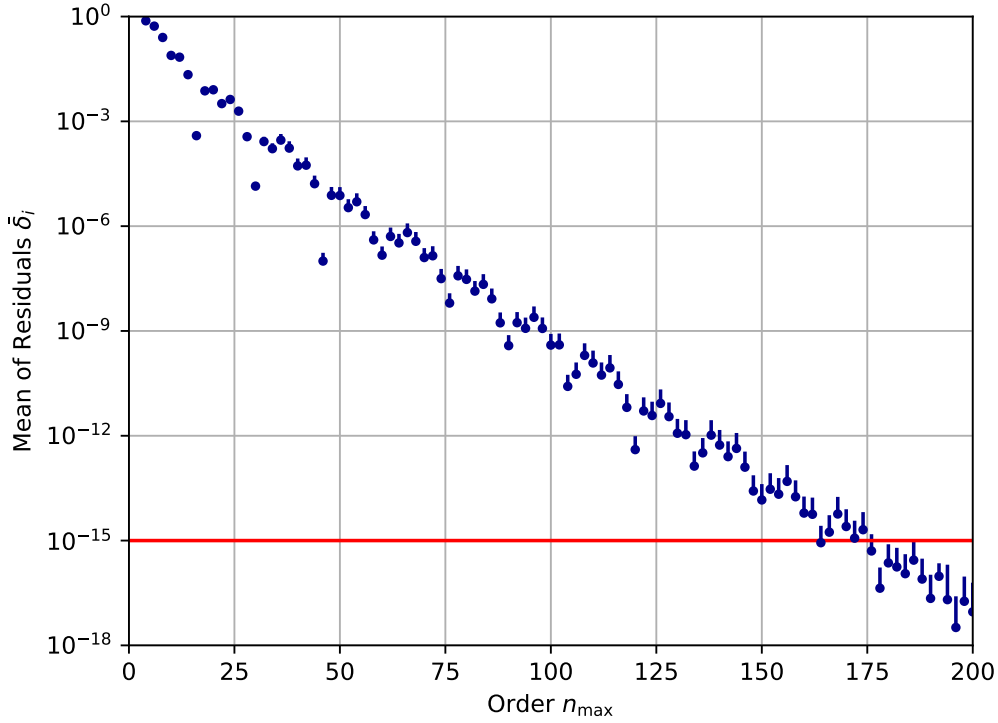


Figure 3.2: Results of the convergence study of the analytically calculated electric potential showing the mean of the residuals $\bar{\delta}_i$ for each iteration i and preceding iteration $i - 1$, enumerating all orders n_{\max} , calculated from the relative residuals δ_i according to Eq. (3.1). All data points are shown with their corresponding 1σ error bars. Although all uncertainties are symmetric, only the upper error bars are plotted for illustrative purposes due to the logarithmic representation. The relative tolerance threshold of $\tau = 10^{-15}$ employed in the COMSOL calculations (cf. Sec. 3.1.1) is depicted in red. The occurrence of outliers is discussed in Ch. 4.

Accuracy of the FEM Numerical Electric Potential Calculations

The raw numerical potential calculated from COMSOL using the model described in Sec. 3.1.1 is benchmarked against the analytical potential (cf. Sec. 2.1.4).

For the subsequent numerical calculations, all points in a cube-like region in the interval $[-1, +1]$ mm for all three cartesian coordinates around the trap center were compared to the analytical solution using a fixed highest order $n_{\max} = 200$, empirically chosen to limit calculation time, but such that the remaining error between orders is well

below $\mathcal{O}(10^{-15})$ (cf. Fig. 3.2), which is equal to the chosen relative tolerance threshold τ used in the COMSOL calculations. The residuals δ were then calculated at each grid point from the numerical simulation in analogy to Eq. (3.1) according to

$$\delta = \left| \frac{U_{\text{analytical}} - U_{\text{numerical}}}{U_{\text{analytical}}} \right|. \quad (3.6)$$

The residuals δ were then binned per volume element onto a cubic lattice with lattice constant a and averaged along a collapsing axis, resulting in the grid of averaged residuals seen in Fig. 3.3. The cubic lattice constant a was empirically chosen as the finest under the condition that every grid point in the resulting grid is filled with at least one value. These residuals were on the order of 10^{-9} on both xy - and xz -plane, being lower around the cylinder-like ROI forced with having a high density of grid points.

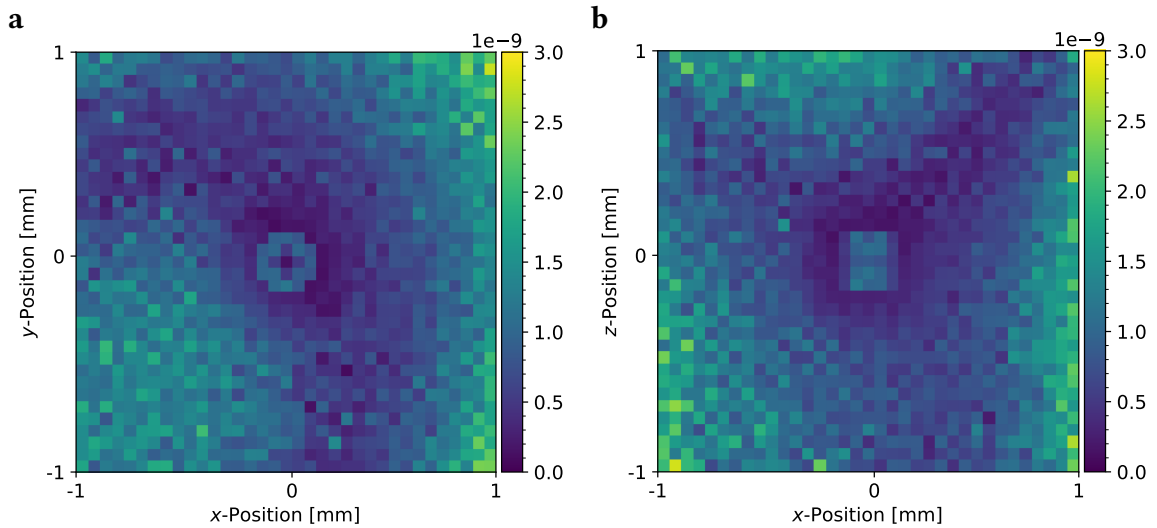


Figure 3.3: Heat maps of the relative residuals δ from Eq. (3.6) between the analytical electric potential and the numerical electric potential from the FEM simulation. All residuals were calculated at the grid points of the numerical potential and then projected and binned (i.e. averaged per volume element along the collapsing axis) onto the **(a)** xy - and **(b)** xz -plane.

Integrity of the Interpolation Methods

For comparing both interpolation methods used in this thesis, namely trilinear interpolation (cf. Sec. 2.2.2) and polynomial regression (cf. Sec. 2.2.3), a number of $N = 100\,000$ interpolation potentials were calculated from points drawn from a uniform distribution in a cube-like space interval with an edge length of 2 mm, located at the center of the trap stack. The resulting interpolated potentials were compared to the analytical potentials (cf. Sec. 2.1.4) at these points with a fixed highest order $n_{\text{max}} = 200$, empirically determined from the calculations presented in Fig. 3.2 up to which the terms of the sum

from Eq. (2.36) were calculated. The residuals δ were then calculated at each point in analogy to Eq. (3.1) according to

$$\delta = \frac{U_{\text{analytical}} - U_{\text{numerical}}}{U_{\text{analytical}}}. \quad (3.7)$$

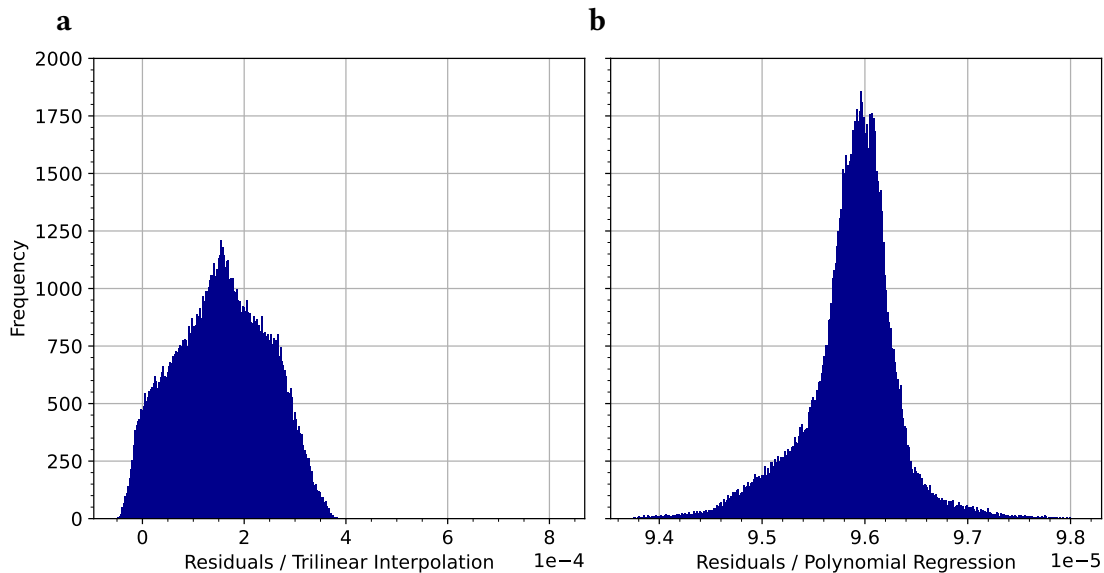


Figure 3.4: Histograms of the residuals δ from Eq. (3.7) of the interpolation methods compared to the analytical potential for a cubic grid. **(a)** Trilinear interpolation and **(b)** polynomial regression used as the interpolation method, and binned to a number of $\lfloor \sqrt{N} \rfloor$ bins for a total of N values. The same cubic grid was used in both underlying FEM simulations to allow direct comparison. To exclude outliers, all values in both histograms were filtered by the *Median Absolute Deviation* criterion (MAD), explained in detail in Refs. [71, 72], using the threshold condition $|\text{MAD}| < 10$. The ranges of the residuals in both histograms were chosen to encompass all values that met the threshold condition. Please note the different scales of the residuals on the abscissas.

Concerning trilinear interpolation, a cubic grid needed to be employed in the interpolation region. It was empirically chosen to be as tightly packed as possible with lattice constant $a = 2 \mu\text{m}$ in a cube with a corner length of 2 mm, without the computing architecture running out of random access memory (RAM). For comparison, the trilinear interpolation and polynomial regression methods were used on the same potential data set, yielding the histograms of the residuals depicted in Fig. 3.4. From the histograms it can be seen that the residuals using the different interpolation methods are comparable in terms of their scale they appear on; both residuals are on the order of 10^{-4} . Interestingly, the dispersion of the distributions are on different orders of magnitude. If only interested in the electric field rather than the electric potential, it is valid to add an arbitrary constant value $c \in \mathbb{R}$ to the potential (cf. *Gauge fixing* [73, 74]), making use of the narrow dispersion of the residuals of the polynomial regression, elevating the accuracy of the residuals to the order of 10^{-5} .

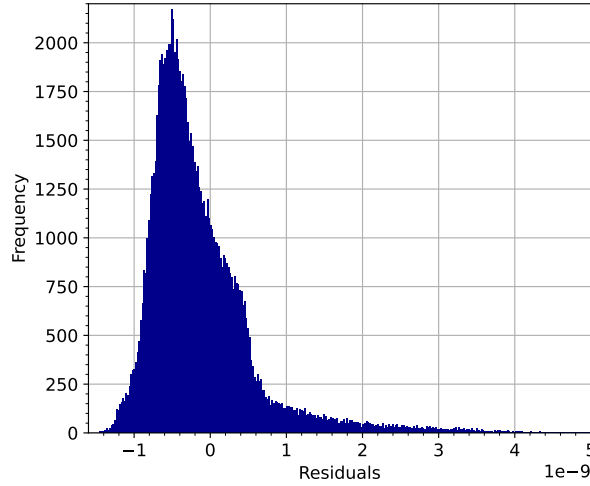


Figure 3.5: Histograms of the residuals δ from Eq. (3.7) using the polynomial regression method with a free tetrahedral grid compared to the analytical potential, binned to a number of $\lfloor \sqrt{N} \rfloor$ bins for a total of N values.

For using polynomial regression, a lattice of arbitrary shape as described in Sec. 3.1.1 was used, resulting in the residuals depicted in Fig. 3.5. It can be inferred that the residuals are on the order of 10^{-9} and therefore roughly five orders of magnitude more precise when compared to the analytical potential. Therefore, polynomial regression along with the free tetrahedral mesh are used exclusively for the remainder of this thesis.

3.2 PENTASIM

In this section, the simulation package PENTASIM is described in terms of its programming framework with the help of an abstracted flow chart and minimal working examples (MWE) of the individual components. This simulation package was implemented for being able to run cylindrical symmetry breaking numerical calculations differing from the analytical solutions, opening the door for the identification of impacts from arbitrarily-shaped radio frequency (RF) excitation and conversion pulses, and electro-magnetic frequency shifts induced by higher orders of the electric potential and magnetic field onto the trapped charged particle.

The simulation package PENTASIM is completely controllable using the interpreted programming language PYTHON, where core functions such as user inputs and input checks, data handling, pre-processing, and simulation management are implemented. By default, the simulation with its time-critical computation steps is outsourced to the compiled programming language JULIA using *Boris' algorithm*, but also allows custom integration algorithms implemented in any other programming language.

3.2.1 Structure

The coarse structure of the simulation can be visualized using the flow chart depicted in Fig. 3.6. It must be noted that all pencil icons represent inputs from the user. If inputs of physical quantities are required, the units are expected to be provided in SI-units (cf. Ref. [75]). All boxes in the flow chart represent classes implemented in PYTHON.

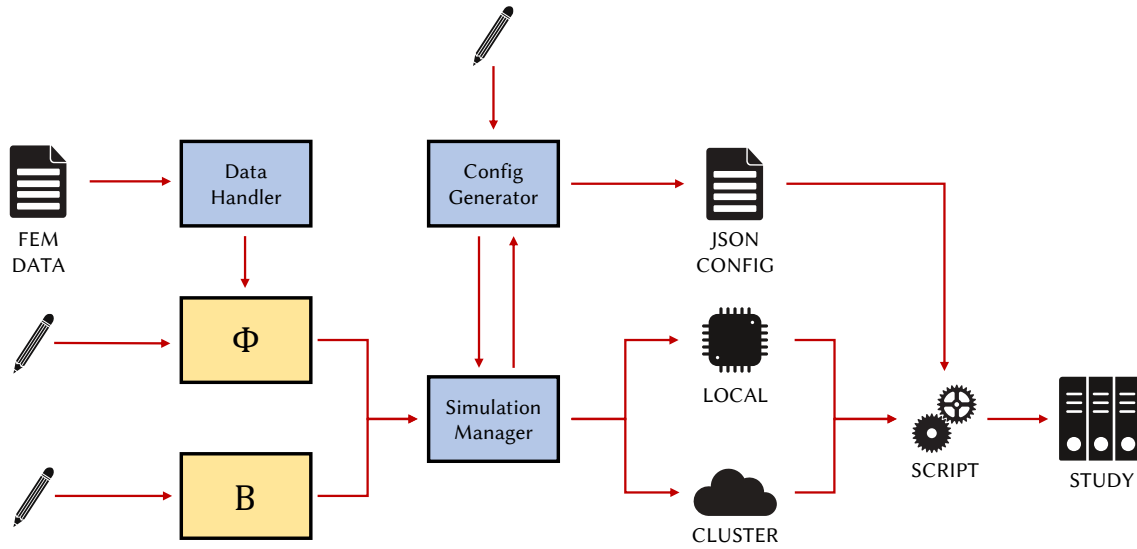


Figure 3.6: Flow chart of the PENTASIM simulation package. User input is represented by pencil icons, whereas implemented classes in PYTHON are depicted as boxes. Starting on the left hand-side, data is fed to the simulation preparation classes Φ and B , which prepare the electric potentials (trap, optionally RF pulses) and the magnetic field for the simulation manager class, requiring further user inputs. If all necessary data is collected by the manager, the simulation is run locally or on the MPIK cluster, saving simulation files for a single simulation or a simulation study to disk.

Electric and Magnetic Preparation Classes Φ and B

Starting from the left hand-side of the flow chart, the preparation classes Φ and B (yellow), representing the electric potential and magnetic field respectively, can be fed from the user by providing the *Taylor expansion* term coefficients C_i [$1/\text{m}^i$] and B_i [T/m^i] from Eqs. (2.17) and (2.20), respectively.

Alternatively, the electric potential class Φ can also be fed by FEM data using the data handler class, whereupon the coefficients C_i are determined by polynomial regression (cf. Sec. 2.2.3) in a user-defined space volume and degree. In addition, when providing multiple FEM data sets, a superposition potential Φ_{SP}

$$\Phi_{\text{SP}}(\mathbf{x}) = \sum_{i=1}^n \Phi_i(\mathbf{x}), \quad (3.8)$$

is calculated, useful e.g. for combining two quarter-electrode data sets to one single half electrode data set. The fit variables up to a degree d are generated by calculating every single combination of $x^i y^j z^k$ without replacement, such that $i+j+k \leq d$ with $i, j, k \in \mathbb{N}_0$. Assuming $d = 2$, this amounts to the fit variables $[1, x, y, z, x^2, xy, xz, y^2, yz, z^2]$. In contrast to the magnetic field class B , the electric potential class Φ can be instantiated once for defining the trap potential, and an arbitrary amount of times for each intended RF pulse.

Configuration Generator and Simulation Manager Class

After electric and magnetic preparation, the configuration generator receives inputs needed for generating the JSON³ configuration file, which includes all information necessary for conducting the simulation. These parameters include the charge and mass state, the initial position and velocity of the charged particle, the DC voltage of the trap, the simulation time steps, and a folder path for storing the results. Optionally a file path to a custom integration algorithm file (and executable command, e.g. "g++") respecting the simulation's JSON file output structure can be stated. After reviewing the completeness and data types of the provided parameters, the class communicates with the simulation manager, where optionally parametric sweep values of one or multiple parameters and information on if the simulation shall be run on the local CPU or on the MPIK cluster is provided. Both local and cluster method are able to run parametric studies parallelly using multithreading. Before calculation, the project structure is determined and all JSON files are created and placed in the respective output folders. The calculation of the simulation is then handed over to the default or provided script, solving the differential equation for advancing the charged particle according to the set parameters. The results of the simulation or study are saved to disk in bunches during the calculation.

JULIA Simulation File

The default simulation file written in the programming language JULIA parses the JSON file string as a command line argument and reads out all necessary parameters for calculating the simulation. After parsing, a static gradient function is calculated from the aforementioned fit variables up to and including the highest occupied (non-zero) coefficient of degree d , being able to calculate the electric field $\mathbf{E}(\mathbf{x})$ at any given position vector \mathbf{x} inside the trap. Then, the integration of the charged particle is performed using *Boris' algorithm* (cf. Sec. 2.2.4). If an RF pulse is specified, its contribution to the electric field is calculated for the current time step and position by a superposition of the trap and RF electric field. When dealing with temporally non-matching values concerning the

³JavaScript Object Notation

simulation time steps and the RF amplitude time steps, a linear interpolation is employed between the RF amplitudes.

3.2.2 Runtime

The simulation runtime was significantly accelerated during the course of this work, which can be attributed in large part to the usage of a compiled language such as JULIA and the exploitation of its capabilities through vectorization, in-place operations, and static arrays that allow the compiler to channel resources more efficiently. In the latest version of PENTASIM, a simulation with a time range of $T = 1$ s and time steps of $\Delta t = 1$ ns takes about 14 min on an office laptop and about 18 min on the MPIK cluster including the simulation preparation in PYTHON and the computation and storage of the solutions in JULIA, resulting in approximately 32 GB of data for one temporal and three spatial 64 bit quantities. The hardware used was a commercial *Dell Latitude 5410* laptop equipped with an *Intel Core i5-10310U* quad-core processor running at a clock rate of 1.7 GHz, with 16 GB random access memory (RAM), and a solid-state drive (SSD).

3.2.3 Minimal Working Examples

In the Appendix, minimal working examples (MWEs) leading through example usages of PENTASIM are shown to demonstrate key features of the simulation and to serve as orientation and quick help. All variables written in capital letters refer to variables that must be filled in by the user. Furthermore, all parameter values used are to be understood as exemplary.

3.3 Benchmarking

In this section, several benchmarks between simulation and theory are carried out for evaluating the integrity and accuracy of the simulated predictions. These benchmarks comprise the temporal and spatial inspection of the motion of the charged particle, the retrieval and comparison of the three independent eigenfrequencies to the analytically expected values, the investigation of frequency shifts induced by electric and magnetic higher order terms, and an examination of the effects of conversion and excitation pulses on the ion's motion.

All simulations shown in this section were conducted using a virtual ${}^{163}_{67}\text{Ho}^{38+}$ ion, which is a commonly used ion at PENTATRAN and a promising candidate for studies of the neutrino mass by probing the ion's electron capture [76]. The initial values for the simulation were set to a position $x_0 = (10, 0, 0)^\top \mu\text{m}$, a velocity $v_0 = (5, 5, 10)^\top \text{ms}^{-1}$ at time step $t_0 \equiv 0$, an electric trap voltage $U_0 = -30$ V, a magnetic field strength $B_0 = 7$ T, and a simulation time step $\Delta t = 10^{-11}$ s, unless otherwise specified.

3.3.1 Ion Motion

To visually examine the motion of the charged particle in the simulation, several plots were created showing the time evolution of all three position variables as well as a top view of the motion projected onto the xy -plane. The combined representation of these plots can be seen in Fig. 3.7, where the temporal range was chosen to correspond to the duration of one magnetron period. In the two plots in the upper half of the figure, it can be seen that the fast modified cyclotron motion modulates the slow magnetron motion. In the diagram on the lower left side of the figure, the axial motion is visible, while the projection on the xy axis in the lower right figure shows the superposition of the radial modes.

3.3.2 Eigenfrequencies

The more accurate a simulation resembles the theoretical solution for given conditions, the higher the value of its predictions and the higher its potential to reveal subtleties which might lead to a better understanding of the processes under investigation. To confirm the integrity and accuracy of its predictions, numerous simulations have been evaluated retrieving the inherent three eigenfrequencies of the system, which are of special interest. For this purpose, numerical integrations of a charged particle were performed to obtain its temporal motion, from which magnetron, axial, and modified cyclotron frequency were extracted by fitting the equations of motion (cf. Eqs. (2.5)-(2.7)) onto the temporal evolution of the x - and z -positions using the *Least Squares Error* (LSE) criterion [77]. For retrieving the global minimum of the LSE function, a concatenation of methods was used. First, the eigenfrequencies were extracted coarsely by determining the maxima in frequency space using the *Fast Fourier Transform* (FFT) [78]. Second, these maxima were used to define boundary regions that delimit the parameter space for the application of *Differential Evolution* (DE) [79, 80] using the LSE criterion for optimization. Third, the results of the DE were refined by a second optimization using the LSE criterion in a narrower parameter space. It was found that the described method is more stable compared to a simple LSE fit, but still susceptible to the choice of the size of the boundary regions, which can lead to instabilities in the fitting.

In a second step, the retrieved eigenfrequencies were compared to the theoretical eigenfrequencies by calculating the residuals δ as

$$\delta = \left| \frac{\nu_{\text{analytical}} - \nu_{\text{fit}}}{\nu_{\text{analytical}}} \right| \quad (3.9)$$

for each eigenfrequency. Since the uncertainties of the determined eigenfrequencies resulting from the square root of the diagonal of the covariance matrix of the fit were several orders of magnitude smaller than the calculated residuals, they were neglected

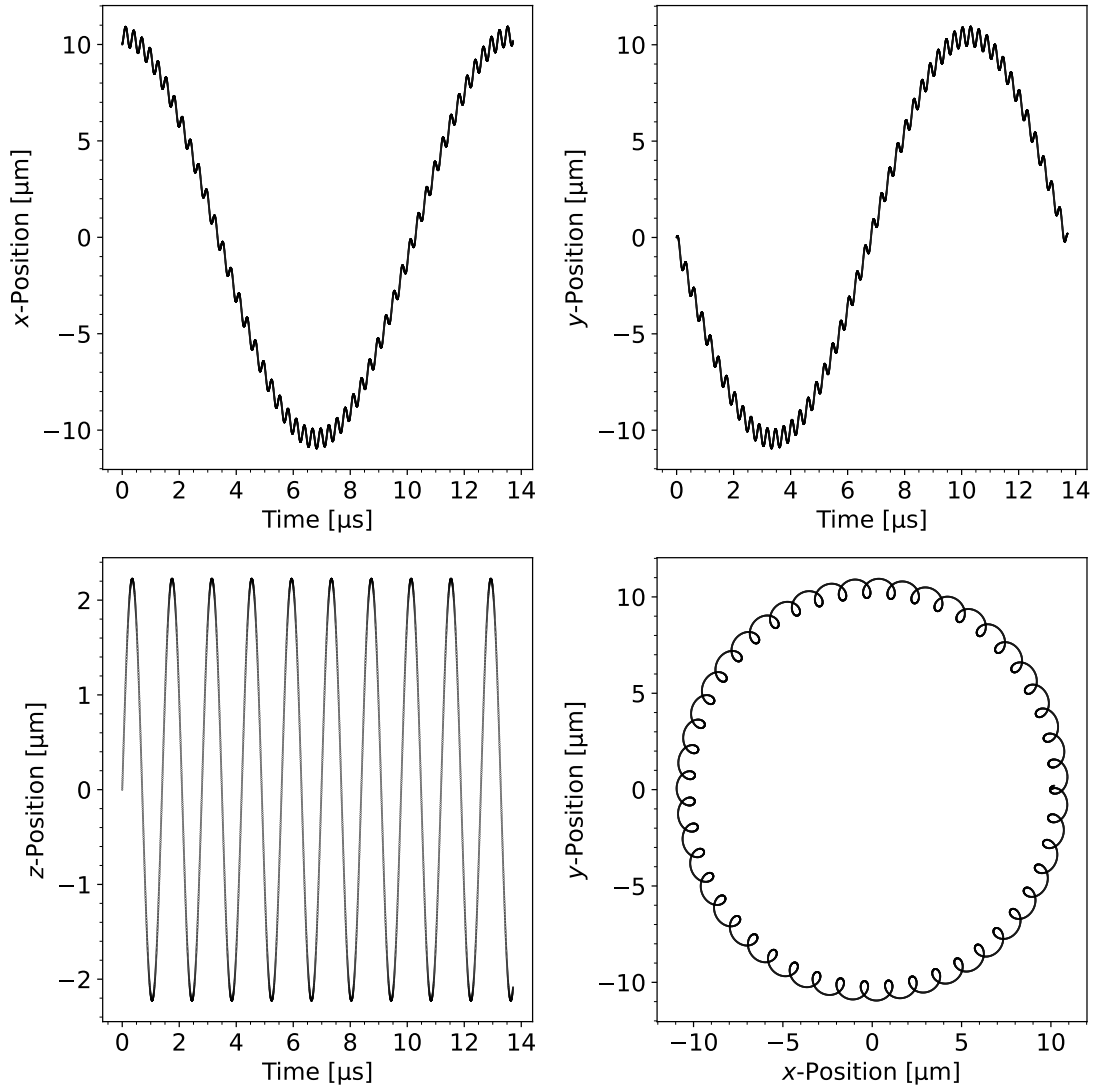


Figure 3.7: Temporally recorded spatial data of ion motion in the simulation under ideal trap conditions, i.e. harmonic electric potential and homogenous magnetic field, for visual verification of the integrity of the predictions. To match the magnitudes of the three eigenfrequencies so that they can be distinguished, the magnetic field strength B_0 was reduced to 1 T for this figure. In the two plots in the upper half of the figure the consist of a superposition of the fast modified cyclotron motion modulating the slow magnetron motion. The diagram on the lower left side of the figure shows the axial motion, while the projection on the xy axis in the lower right figure shows the superposition of the radial modes.

in all considerations. In Fig. 3.8, the residuals of the eigenfrequencies compared to the theoretical solutions (cf. Eqs. (2.8) and (2.9)) are depicted against the simulation time step Δt . The expectations agree with the results, as a decrease of the time step Δt is anticipated to lead to an increase in accuracy of all eigenfrequencies. For simulation time steps smaller than 5×10^{-11} s, the retrieved magnetron frequency shows inconsistencies in terms of its behavior compared to both other eigenfrequencies. This effect is discussed

in Ch. 4. All relative residuals δ range from 10^{-2} to 10^{-15} indicating that the residuals are strongly dependent on the simulation time step Δt , which was examined in a range from 10^{-9} s to 10^{-12} s.

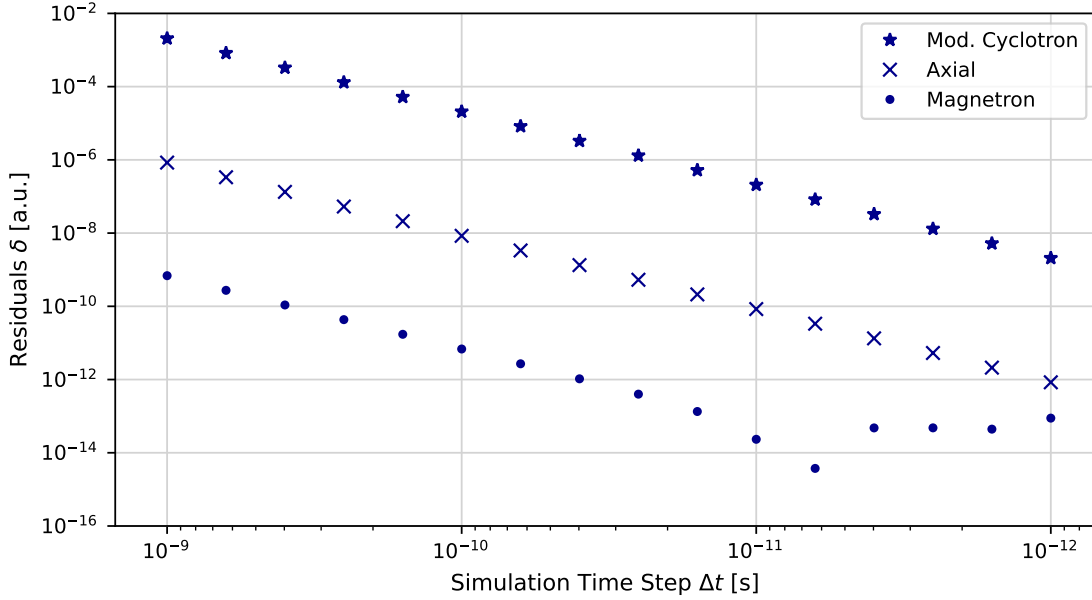


Figure 3.8: Residuals of the determined eigenfrequencies (magnetron, axial, and modified cyclotron) compared to the expected theoretical eigenfrequencies obtained using Eq. (3.9) as a function of the simulation time step Δt .

3.3.3 Electro-Magnetic Frequency Shifts

To further investigate the integrity of the simulation, frequency shifts induced by electric and magnetic higher order terms predicted by theory [43] were chosen for benchmarking. For this purpose, studies were conducted varying the 4th order electric potential coefficient C_4 and the 2nd order magnetic field coefficient B_2 . The eigenfrequencies of these simulations were extracted by LSE fitting of the equations of motion, analogue to the description provided in Sec. 3.3.2. As aforementioned, the uncertainties yielded from fitting were neglected since they were several orders of magnitude lower than the retrieved frequency shifts.

In Fig. 3.9, the electrically induced relative frequency shifts are plotted and compared to the analytical predictions from Eqs. (2.18) and (2.19). The frequency shifts are calculated with respect to the eigenfrequencies and the amplitudes of the charged particle in absence of the electric coefficient C_4 . The values of the C_4 coefficients were chosen such that the smallest relative frequency shift would occur on the order of 10^{-9} , several orders of magnitude above the estimation uncertainty of the fitting parameters. The experimentally acquired data fits well to the expected theoretical values. In addition to the visual review,

a linear fit of the experimental data confirmed the slopes of experimental data and theory to be identical within their margins of error.

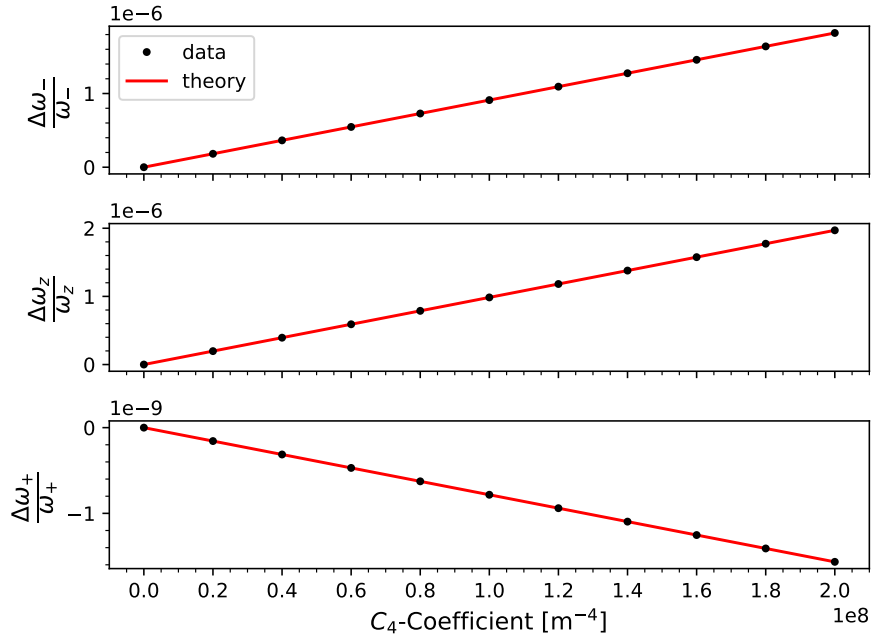


Figure 3.9: Electrically induced relative frequency shifts compared to the theoretical expectation (red) by changing the fourth-order electric coefficient C_4 . All three eigenfrequencies ω_- , ω_z , and ω_+ (magnetron, axial, and modified cyclotron, respectively) were obtained through LSE fitting of the equations of motion.

In Fig. 3.10, the magnetically induced frequency shifts are plotted and compared to the analytical predictions from Eqs. (2.21)-(2.23). The values of the B_2 coefficients were chosen such that the smallest relative frequency shift would occur on the order of 10^{-9} , several orders of magnitude above the estimation uncertainty of the fitting parameters. The visual conformity of the experimental data and the theoretical expectations was further examined by comparing the slopes of experimental data retrieved by a linear fit to theory. It was found that all slopes agree to theory within their margins of error, matching the theoretical expectations.

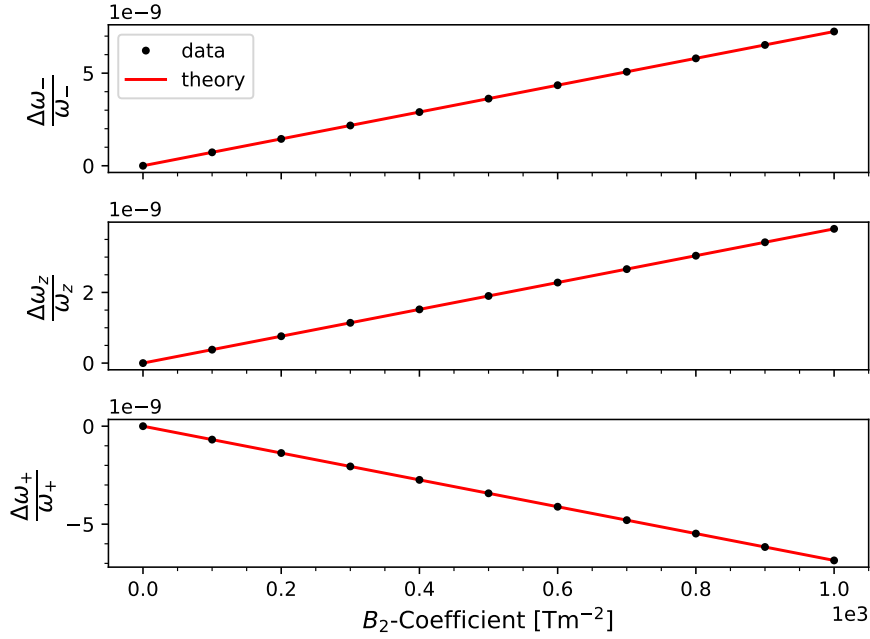


Figure 3.10: Magnetically induced relative frequency shifts compared to the theoretical expectation (red) by changing the second-order magnetic coefficient B_2 . All three eigenfrequencies ω_- , ω_z , and ω_+ (magnetron, axial, and modified cyclotron, respectively) were obtained through LSE fitting of the equations of motion.

3.3.4 Excitation and Conversion Pulses

Excitation and conversion pulses constitute a powerful tool for controlling the motion of the charged particle inside the trap. A simulation allowing access to the application of pulses with arbitrary shapes opens up possibilities to test new measurement and controlling schemes. Therefore, the prediction of the behavior of the charged particle during an RF pulse of arbitrary shape was subject to this simulation package.

In this section, an exemplary dipole pulse is applied, whose response is shown qualitatively in Fig. 3.11. For this simulation, a sinusoidal dipole pulse with an RF frequency matching the axial frequency was applied in z -direction with a voltage of 5 kV according to Eq. (2.25). Although such high voltages are not normally used in the experiment, the magnitude was chosen to show amplitude reduction and magnification with a phase offset of π , which serves as proof of principle for dipole excitation with an ideal electric potential.

Corresponding studies were also carried out using sinusoidal quadrupole pulses, converting energy from the modified cyclotron mode to the axial mode and vice versa. In this section, an exemplary quadrupole pulse is applied, whose response is shown qualitatively in Fig. 3.12. For this simulation, a sinusoidal quadrupole pulse with an electric field amplitude of 10^5 Vm^{-1} and an RF frequency matching the lower side band frequency of the axial and modified cyclotron motion was applied, calculated with the

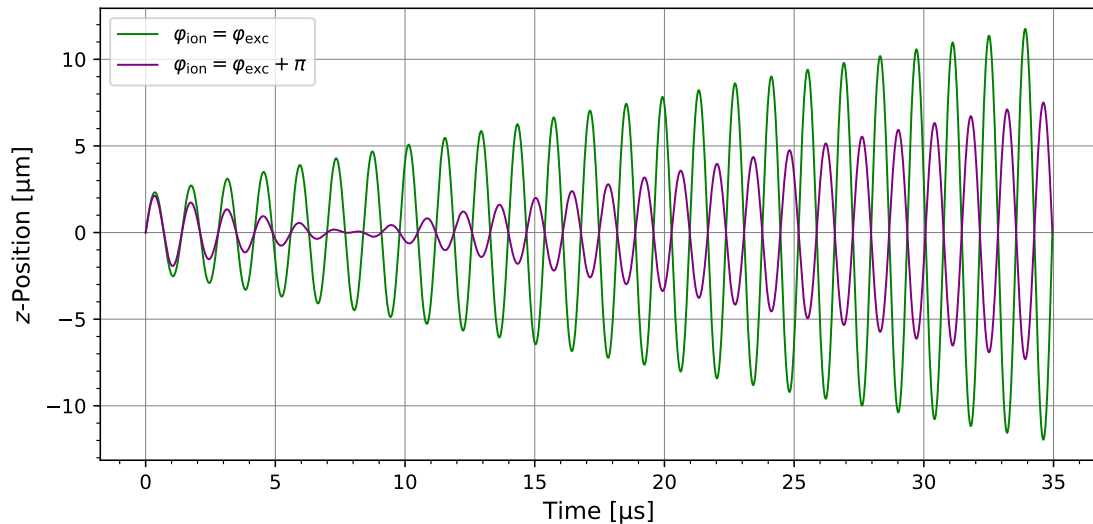


Figure 3.11: Simulation of an in-phase (green) and an opposite-of-phase (purple) dipole excitation pulse using an ideal electric potential, altering the axial motion of the charged particle. The effect of amplitude reduction and increase with phase offset of π has been investigated in Ref. [45].

extracted frequencies at the corresponding simulation time step from the results of the fits in Sec. 3.3.2. Although such high electric field amplitudes are not normally used in the experiment, the magnitude was chosen to allow for illustration of multiple Rabi cycles during the chosen time interval, serving as proof of principle for quadrupole excitation with an ideal electric potential. The Rabi frequency was compared to the expected value from theory, extracted by manually counting the number of cycles in a given time period. The Rabi frequency from the simulation was found to agree with the theoretical value, calculated using Eq. (2.30), within the error limits.

In addition to the ability to apply RF pulses using an ideal electric potential, as described in the previous paragraph, the simulation also provides the ability to read in potentially cylindrical symmetry breaking electric potentials generated by FEM calculations. To illustrate the integrity of these predictions, an FEM-generated electric dipole potential in x -direction was calculated by applying a phase difference of π between two opposing segments of the RE using the model described in Sec. 3.1.1. For this simulation, whose results are shown in Fig. 3.13, a sinusoidal dipole pulse in x -direction was applied with a voltage of 1 kV using the retrieved electric potential coefficients by polynomial regression. Although such high voltages are not normally used in the experiment, the magnitude was chosen to show amplitude reduction and magnification with a phase offset of π , which serves as proof of principle for dipole excitation using an FEM-generated electric potential.

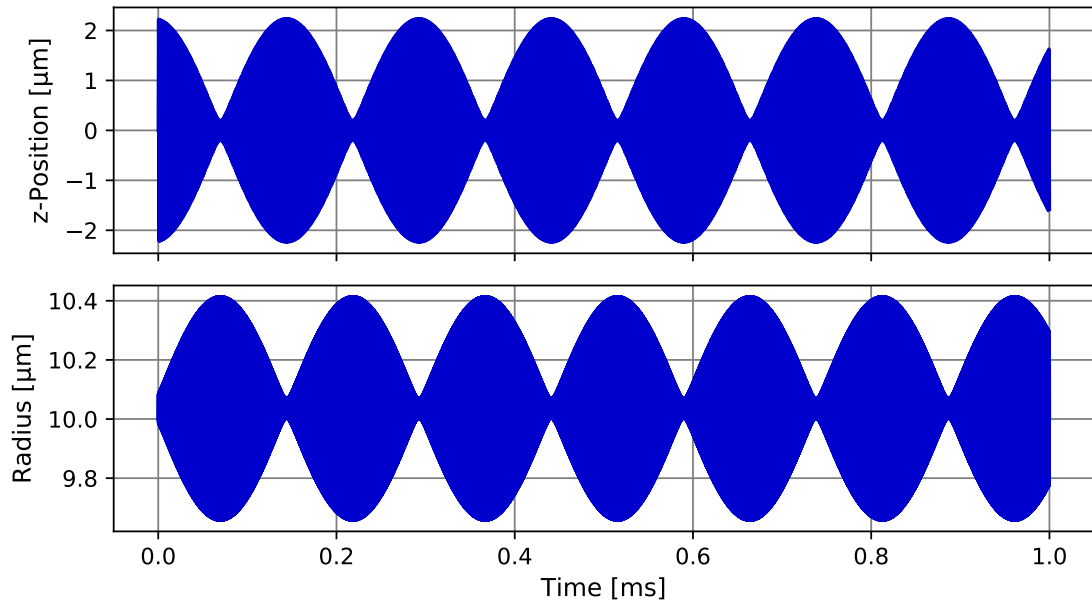


Figure 3.12: Simulation of a quadrupole conversion pulse using an ideal electric potential, exchanging energy between the axial mode (upper plot) and the modified cyclotron mode (lower plot), where the radius refers to the motion in the xy -plane. The effect of amplitude reduction and increase using quadrupole pulses has been investigated in Ref. [81].

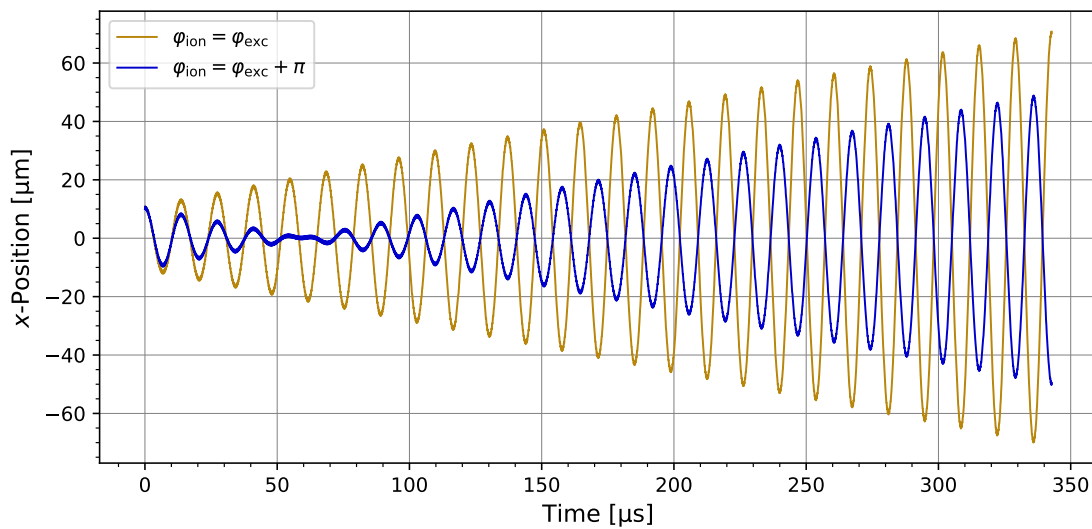


Figure 3.13: Simulation of an in-phase (golden) and an opposite-of-phase (blue) dipole excitation pulse using an FEM-generated electric potential, altering the magnetron motion of the charged particle. The effect of amplitude reduction and increase with phase offset of π has been investigated in Ref. [45].

Chapter 4

Discussion

The objective of this work was to create a simulation package capable of simulating the motion of a charged particle confined in a Penning trap for studying systematic effects and the influence of arbitrarily shaped excitation and conversion pulses. To achieve this, the electric potential was used in a polynomial expansion representation that is not constrained by cylindrical symmetry. The *Finite Element Method* (FEM), a state-of-the-art method able to numerically approximate electric potentials in volumes between arbitrarily shaped electrodes, was selected as a suitable method.

In order to investigate the accuracy of these numerical approximations, an FEM model was implemented based on an already known model for which an analytical solution exists, allowing for a direct comparison. First, the convergence of the analytical electric potential calculations was quantitatively investigated. For this purpose, the electric potential was evaluated on numerous randomly chosen points inside a region of interest (ROI), taking into account increasingly higher orders of sum terms. Relative residuals of the electric potentials were then calculated between each pair of points from adjacent orders, confirming the convergence of the analytical potential calculations with higher orders as expected. A regular pattern of outliers was observed not explainable by the uncertainties of the values. The reason might be that the used analytical electric potential is a representation of oscillating terms. If adjacent terms occur to be similar in terms of their magnitude, they more or less cancel each other out, leaving the residuals to drop occasionally. From the consideration of the analytical electric potential, for computational time reasons, the highest computational order was set to a value of 200 for the remainder of this work so that the calculations fall below the specified accuracy threshold from the FEM simulations discussed below.

To spatially test the accuracy of the FEM-generated electric potential at the mesh points provided by COMSOL, relative residuals of the electric potential at all mesh points inside a ROI were calculated using the aforementioned analytical electric potential solution. After grouping the mesh grid points into bins using their location on the xy - and xz -plane, the absolute mean of the residuals was visualized. The result implies that all

residuals are of the order of 10^{-9} , being lower around the edges of the cylindrical space, which was introduced to incorporate a high density of mesh grid points in the center. The question arises as to why the residuals are closer to the expected solution around the space interval with high mesh grid density, rather than inside this space. An explanation for this might lie in the fact that, due to the rigid geometry of the employed cylinder, additional boundary conditions were introduced on its surface. It is expected that the curved areas of the cylinder barrel and the sharp edges around the edge of its cover are difficult to model. In the future, additional studies should be carried out experimenting with different forced mesh geometries. Also, an interesting approach would be to force the mesh to get finer towards the center of the trap without the introduction of additional geometries, taking curved or sharp boundary conditions out of the equation. Nevertheless, all observed residuals remain within a reasonable range. A study with a completely free tetrahedral mesh without the introduction of forced high density spaces resulted in less grid points being placed towards the center of the trap, leading to a decreased prediction accuracy of the FEM. The relative density of mesh grid points is determined automatically by the used FEM algorithm, increasing the number of grid points in regions where the gradient of the electric potential is highest. As the center of the trap is located far from the electrodes compared to the rest of the volume, the least amount of mesh grid points is placed in the region where a high accuracy is demanded. Therefore, a user-defined high density zone in the center of the trap was found to be crucial in terms of the FEM's accuracy.

Opposed to the discrete approximated solution from the FEM calculations, a continuous representation of the electric potential is necessary for integrating the equations of motion. Therefore, a method interpolating between known values at mesh grid points was required. The two methods of choice were trilinear interpolation and polynomial regression, using two different approaches for interpolation; the former uses solely mesh grid points around the unknown point, whereas the latter takes all points inside a chosen space region into account. For determining their accuracy, both methods were benchmarked against the known analytical solution of the electric potential. As the trilinear interpolation needs to be applied to a cubic grid, both methods were compared directly using the same regular grid. Numerous random points were drawn for which relative residuals to the analytical solution were calculated. Investigation of the distribution of the residuals revealed that the residuals of both methods are of order 10^{-4} , but their dispersions are on different orders of magnitude. Concentrating on the electric field rather than the electric potential, it is valid to add an arbitrary constant value $c \in \mathbb{R}$ to the potential, exploiting the ambiguity of the electric potential from *Gauge fixing*. Then, the narrow dispersion of the residuals of the polynomial regression elevate the accuracy of the residuals to the order of 10^{-5} . Thus, polynomial regression still outperforms trilinear interpolation by an order of magnitude. One reason for this could be that the ideal

electric potential in a Penning trap is given by second order parabolic terms that cannot be represented using trilinear interpolation, since this method only interpolates linearly in every dimension. The free tetrahedral mesh, interpolated using polynomial regression, revealed residuals on the order of 10^{-9} , the same order of magnitude as found in direct comparison of the FEM solution at its grid points to the analytical expression. Therefore, it can be assumed, that polynomial regression is an adequate method for interpolation between grid points of the FEM simulation. As polynomial regression can be expanded to any order and space, it must be noted that it is necessary to constrain both parameters such that under- and overfitting remain in a tolerable range. In addition, polynomial regression is superior to trilinear interpolation in terms of calculation speed, since the derivation of a functional expression of the electrical potential eliminates the need to access the FEM simulation file continually. On the other hand, for each value calculated by trilinear interpolation, eight surrounding corner points of the electric potential need to be fetched from the FEM simulation file.

For putting the simulation through its paces, the integrity and accuracy of its predictions was investigated by various steps. First, the ion's motion was examined qualitatively by generating diagrams of the motion of the charged particle for all three cartesian coordinates and in the xy -plane for one magnetron cycle, where all eigenmotions could be visually identified. Second, the eigenfrequencies from the simulation were investigated quantitatively for measuring the accuracy of the eigenfrequencies by comparing them to the theoretical values. This step required the development of a method for retrieving the eigenfrequencies. By conducting empirical trials, a combination of *Fast Fourier Transform* (FFT), *Differential Evolution*, and *Least Squares Error* (LSE) fitting of the equations of motion for a charged particle inside a Penning trap was found to be most effective and stable in retrieving the eigenfrequencies. Using this method, all eigenfrequencies were retrieved for simulations using ideal trapping conditions, making them directly comparable to theoretical expectations. For investigating the simulation's predictions for different simulation time steps in the integration, all eigenfrequencies were extracted over roughly three orders of magnitude and compared to theory by calculating relative residuals with the theoretically expected frequencies. In line with the expectations, the study indicated that the residuals of the eigenfrequencies decrease exponentially with decreasing simulation time step. The most precise frequency was the magnetron frequency, followed by the axial frequency and the modified cyclotron frequency, respectively. It must be noted that the succession of precision corresponds to the magnitude of the frequencies, i.e. the higher the frequency, the worse its accuracy in the simulation. In the case of circular motion, the higher the frequency, the shorter the period of oscillation, and the fewer the number of sampling points recorded by the integration per revolution. A circle can be represented mathematically as an infinite number of infinitesimal adjacent lines. Due to the finite simulation time step, only a finite number of adjacent lines can be used to

represent the circle, leading to inconsistencies that increase in magnitude for a decrease in the sample points per orbital revolution. Therefore, as expected, the higher the frequency, the less accurate its value can be retrieved by an integration algorithm. To investigate the integrity of the frequency determination method, motivated by the unexpected jump in residuals in the magnetron frequency, reduced χ^2 values were calculated for all fits. However, since no sudden jump in the χ^2 values was found, there was no indication that the four values did not converge at the lower end of the observed simulation time step range. Also, it was found that the relative retrieval error of the magnetron frequency remained two orders of magnitude lower than the lowest retrieved residual. Due to these reasons, it can be assumed that this unexpected behavior in the magnetron frequency arises from the simulation itself. This behavior should be further investigated in future studies, presented in detail in Ch. 5.

For experimentally confirming the predicted frequency shifts induced by higher order electric and magnetic terms in the simulation, ion integrations for varying values of C_4 and B_2 were run with the goal to compare the slopes to the theoretically predicted value using the already described frequency extraction method. Then, linear fits using the LSE criterion were calculated, and the slopes were compared to the theoretically predicted values. For both studies and all eigenfrequencies, the experimentally retrieved frequencies agreed within their margins of error with the predicted frequency shifts. For investigating the effects of radio frequency (RF) excitation and conversion pulses on the motion of the charged particle in both an ideal, and an FEM-generated electric potential, dipole and quadrupole pulses were applied. For the dipole case, two simulations were run using an in-phase and opposite-of-phase pulse. The experimental observations agree with the theoretical expectations. The investigation of the quadrupole case confirmed the Rabi frequency of the beating between the axial and the modified cyclotron mode to be in line with the expected theoretical value within the margin of error.

Last but not least, the limitations of the simulation were found to arise from the value of the simulation time step which is needed to be sufficiently low for retrieving key characteristics of the experiment with high accuracy.

Chapter 5

Conclusion and Outlook

The goal of this thesis was to develop a simulation package for studying systematic effects and excitation and conversion pulses of arbitrary shape. For this purpose, PENTASIM was implemented to calculate trajectories of charged ions in static or dynamic, non-symmetric, electric potentials.

The objective of this thesis was to set a foundation for the study of the aforementioned effects by creating a simulation tool capable of studying these effects, and to quantify the accuracy of the simulation's predictions. Therefore, multiple studies were carried out to investigate the precision of the simulations by comparison with theory. These studies comprised testing of convergence of the analytical electric potential solution, testing of the accuracy of the FEM-generated electric potential calculations, testing of the integrity of two implemented interpolation methods, testing of the examination of the ion's motion and eigenfrequencies compared to theory, quantitatively investigating electro-magnetic frequency shifts predicted by theory, and qualitatively probing dipole and quadrupole excitation pulses.

The examination of the FEM-generated electric potential indicated that further studies should be carried out focusing on the effects of the spatial mesh distribution for optimizing the accuracy of the approximation in the region where the ion traverses.

Finding a suitable order of fit for polynomial regression and a suitable spatial interval is currently the task of the experimentalists. The provision of goodness measures like the calculation of confidence intervals and hypothesis tests would result in a more informed choice of these parameters.

By benchmarking the eigenfrequencies of the integrated motion it was indicated that a reasonably high number of sample points per time frame is necessary for increasing the accuracy of the simulation to a range usable for experimental studies. Also, the simulation time step cannot be reduced arbitrarily, due to limits in calculation time. Therefore, further studies should be directed towards investigating the behavior of the accuracy of the eigenfrequencies using even smaller time steps, and to probe whether the exponential decrease in the residuals of the eigenfrequencies is curbed at some point

using the 2nd order *Boris algorithm* [60]. Initial studies indicated that the explicit 4th order symplectic integrator called *Explicit Symplectic Shadowed Runge–Kutta* (ESSRK), published and analyzed in Refs. [82, 83], is expected to provide a higher accuracy using a lesser amount of sample points per time frame, potentially leading to a more precise and efficient simulation.

In general, addition of time-varying electric potentials and magnetic fields for studying drift effects, patch potentials and noise on the electrodes, image charge effects, relativistic effects, methods used in the experiment such as the phase shift method, and the interaction of the ion with a resonator would be of additional value and further extend the simulation tool kit PENTASIM.

Appendix

Code Block A.1: Load an FEM-generated electric potential from a text file from COMSOL, or load and superimpose multiple normalized simulation files to a single electric potential. Afterwards, the electric potential can be prepared for usage in the simulation by applying polynomial regression, calculating the polynomial feature coefficients for a given `degree` and `fit_range`. An RF pulse can be added by reading in additional FEM data or by setting a dipole or quadrupole pulse potential by passing the indices of the participating eigenvectors using `pulse_direction`.

```
1 from pentasim.potential.electric_potential_preparation \
2     import DataHandler, ElectricPotentialPreparation
3
4 single_path = "<YOUR_FILE_PATH>/fem_file.txt"
5 fem_data = DataHandler(file_paths=single_path)
6
7 multiple_paths = [ "<YOUR_FILE_PATH>/fem_file_1.txt",
8                   "<YOUR_FILE_PATH>/fem_file_2.txt",
9                   "<... >",
10                  "<YOUR_FILE_PATH>/fem_file_n.txt" ]
11 superimposed_fem_data = DataHandler(file_paths=multiple_paths)
12
13 electric_potential = ElectricPotentialPreparation(degree=4,
14                                                  data=fem_data)
15 electric_potential.fit(fit_range=(-1e-3, +1e-3))
16
17 el_dipole_potential = ElectricPotentialPreparation(degree=2)
18 el_dipole_potential.set_pulse(pulse_direction="x")
19
20 el_quadrupole_potential = ElectricPotentialPreparation(degree=2)
21 el_quadrupole_potential.set_pulse(pulse_direction="xz")
```

Code Block A.2: Typesetting arbitrary C_i and B_i coefficients to the simulation using example values.

```
1 from pentasim.potential.electric_potential_preparation \
2     import ElectricPotentialPreparation
3 from pentasim.potential.magnetic_field_preparation \
4     import MagneticFieldPreparation
5
6 electric_potential = ElectricPotentialPreparation()
7 magnetic_field = MagneticFieldPreparation()
8
9 electric_potential.add_coefficients({"C2": 1e4,      # [1/m^2]
10                                     "C4": 1e-8,     # [1/m^4]
11                                     "C6": 1e-12,    # [1/m^6]
12                                     })
13
14 magnetic_field.add_coefficients({"B0": 7.,         # [T]
15                                   "B1": 1e-3,     # [T/m]
16                                   "B2": 1e-5,     # [T/m^2]
17                                   })
```

Code Block A.3: Example of typesetting all other necessary input parameters for the simulation. Either Code Block A.1 or Code Block A.2 is assumed for this Code Block. The parameters `mass_state` (u) and `charge_state` (eAs) can be interchanged with the parameters `mass` (kg) and `charge` (As). It must be noted that multiple RF-pulses with different RF parameters as well as multiple parameter studies for every parameter of the simulation may be added. The simulation in this example is run on the cluster, but can also be run locally setting `option="local"`.

```

1 from pentasim.simulation.simulation_preparation \
2     import SimulationPreparation
3 from pentasim.simulation.numerical_simulation \
4     import SimulationManager
5
6 ion = {
7     "mass_state": 9.,
8     "charge_state": 1.,
9     "pos_init": [10e-6, 0., 0.],
10    "vel_init": [1., 1., 1.],
11    }
12
13 trap = {
14    "dc_voltage": -30,
15    "el_coefficients": electric_potential.coefficients,
16    "mag_coefficients": magnetic_field.coefficients,
17    }
18
19 config = {
20    "sim_t_range": (0., 1., 1e-10),
21    "path_output_config": "/<YOUR_SIM_OUTPUT_FOLDER_PATH>/",
22    "save_output_flag": True,
23    }
24
25 rf = {
26    "rf_t_range": (0.4, 0.6),
27    "rf_times": rf_times,
28    "rf_voltages": rf_voltages,
29    "rf_coefficients": el_potential_rf.coefficients
30    }
31
32 config_generator = ConfigGenerator()
33
34 config_generator.add(mode="Ion", parameters=ion)
35 config_generator.add(mode="Trap", parameters=trap)
36 config_generator.add(mode="Config", parameters=config)
37
38 config_generator.add(mode="RFPulse", parameters=rf)

```

```
39
40 study_parameters = [(0., 1., dt) for dt in [1e-9, 1e-10, 1e-11]]
41 simulation.add_study(parameter_mode="Config",
42                      parameter_name="sim_t_range",
43                      parameter_values=study_parameters)
44
45 simulation = SimulationManager(config_generator=config_generator,
46                               executable="julia")
47
48 simulation.run(option="cluster")
```


References

- [1] Jens Dilling, Klaus Blaum, Maxime Brodeur, and Sergey Eliseev. Penning-Trap Mass Measurements in Atomic and Nuclear Physics. *Annu. Rev. Nucl. Part. Sci.*, 68(1):45–74, oct 2018.
- [2] T. Yamaguchi, H. Koura, Yu.A. Litvinov, and M. Wang. Masses of exotic nuclei. *Prog. Part. Nucl. Phys.*, 120:103882, sep 2021.
- [3] Noriaki Ohmae, Masao Takamoto, Yosuke Takahashi, Motohide Kokubun, Kuniya Araki, Andrew Hinton, Ichiro Ushijima, Takashi Muramatsu, Tetsuo Furumiya, Yuya Sakai, Naoji Moriya, Naohiro Kamiya, Kazuaki Fujii, Ryuya Muramatsu, Toshihiro Shiimado, and Hidetoshi Katori. Transportable Strontium Optical Lattice Clocks Operated Outside Laboratory at the Level of 10^{-18} Uncertainty. *Adv. Quantum Technol.*, 4(8):2100015, aug 2021.
- [4] Simon Rainville, James K. Thompson, and David E. Pritchard. An Ion Balance for Ultra-High-Precision Atomic Mass Measurements. *Science (80-.)*, 303(5656):334–338, jan 2004.
- [5] Guangxiang Wu, R. Graham Cooks, Zheng Ouyang, Meng Yu, William J. Chappell, and Wolfgang R. Plass. Ion Trajectory Simulation for Electrode Configurations with Arbitrary Geometries. *J. Am. Soc. Mass Spectrom.*, 17(9):1216–1228, 2006.
- [6] Raymond E March. Quadrupole ion trap mass spectrometry: theory, simulation, recent developments and applications. *Rapid Commun. Mass Spectrom.*, 12(20):1543–1554, oct 1998.
- [7] Jessica M. Higgs and Daniel E. Austin. Simulations of ion motion in toroidal ion traps. *Int. J. Mass Spectrom.*, 363(1):40–51, 2014.
- [8] P. Chauveau, K. Hauschild, A. Lopez-Martens, M. MacCormick, E. Minaya Ramirez, P.G. Thirolf, and C. Weber. Simulations of the novel double-Penning trap for MLLTRAP: Trapping, cooling and mass measurements. *Nucl. Instruments Methods Phys. Res. Sect. A Accel. Spectrometers, Detect. Assoc. Equip.*, 982(June):164508, dec 2020.

- [9] Marc Schuh. *Simulations of the electrostatic and magnetic field properties and tests of the Penning-ion source at THE-Trap*. Master thesis, Ruprecht Karl University of Heidelberg, 2014.
- [10] Y.L. Sun, Y.L. Tian, W.X. Huang, J.Y. Wang, Y.S. Wang, J.M. Zhao, and Y. Wang. Numerical and graphical description on the ion motions in a Penning trap for mass measurements. *Nucl. Instruments Methods Phys. Res. Sect. A Accel. Spectrometers, Detect. Assoc. Equip.*, 724:83–89, oct 2013.
- [11] Huang Wen-Xue, Wang Jun-Ying, Wang Yue, Tian Yu-Lin, Zhu Zhi-Chao, Xu Hu-Shan, and Xiao Guo-Qing. Simulation of the Lanzhou Penning Trap LPT. *Chinese Phys. C*, 33(S1):193–195, mar 2009.
- [12] Jorge A. Diaz, Clayton F. Giese, and W. Ronald Gentry. Sub-miniature ExB sector-field mass spectrometer. *J. Am. Soc. Mass Spectrom.*, 12(6):619–632, jun 2001.
- [13] C. Marinach, A. Brunot, C. Beaugrand, G. Bolbach, and J.C. Tabet. Simulation of ion beam and optimization of orthogonal tandem ion trap/reflector time-of-flight mass spectrometry. *Int. J. Mass Spectrom.*, 213(1):45–62, jan 2002.
- [14] Raymond E. March and John F. J. Todd. *Practical Aspects of Ion Trap Mass Spectrometry: Fundamentals of Ion Trap Mass Spectrometry*. CRC Press, Boca Raton, FL, 3 edition, 1995.
- [15] Dale W. Mitchell. Realistic simulation of the ion cyclotron resonance mass spectrometer using a distributed three-dimensional particle-in-cell code. *J. Am. Soc. Mass Spectrom.*, 10(2):136–152, feb 1999.
- [16] Xinzhen Xiang, Shenheng Guan, and Alan G. Marshal. Simulated ion trajectory and induced signal in ion cyclotron resonance ion traps. *J. Am. Soc. Mass Spectrom.*, 5(4):238–249, apr 1994.
- [17] P. H. Dawson and N. R. Whetten. Ion Storage in Three-Dimensional, Rotationally Symmetric, Quadrupole Fields. I. Theoretical Treatment. *J. Vac. Sci. Technol.*, 5(1):1–10, jan 1968.
- [18] J. Franzen. Simulation study of an ion cage with superimposed multipole fields. *Int. J. Mass Spectrom. Ion Process.*, 106(C):63–78, may 1991.
- [19] F. Vedel, J. André, M Vedel, and G Brincourt. Computed energy and spatial statistical properties of stored ions cooled by a buffer gas. *Phys. Rev. A*, 27(5):2321–2330, may 1983.

- [20] F Vedel and J. André. Influence of space charge on the computed statistical properties of stored ions cooled by a buffer gas in a quadrupole rf trap. *Phys. Rev. A*, 29(4):2098–2101, apr 1984.
- [21] M. Schuh, F. Heiße, T. Eronen, J. Ketter, F. Köhler-Langes, S. Rau, T. Segal, W. Quint, S. Sturm, and K. Blaum. Image charge shift in high-precision Penning traps. *Phys. Rev. A*, 100(2):1–17, 2019.
- [22] Marc Schuh. *Simulations of the image charge effect in high-precision Penning traps and the new IGISOL ion buncher*. Phd thesis, Ruprecht Karl University of Heidelberg, 2019.
- [23] Christian Will, Matthew Anders Bohman, Thomas Driscoll, Markus Wiesinger, Fatma Abbass, Matthias Joachim Borchert, Jack Alexander Devlin, Stefan Erlewein, Markus Fleck, Barbara Latacz, Ron Moller, Andreas Mooser, Daniel Popper, Elise Wursten, Klaus Blaum, Yasuyuki Matsuda, Christian Ospelkaus, Wolfgang Quint, Jochen Walz, Christian Smorra, and Stefan Ulmer. Sympathetic cooling schemes for separately trapped ions coupled via image currents. *New J. Phys.*, feb 2022.
- [24] S. Van Gorp, M. Beck, M. Breitenfeldt, V. De Leebeeck, P. Friedag, A. Herlert, T. Iitaka, J. Mader, V. Kozlov, S. Roccia, G. Soti, M. Tandeki, E. Traykov, F. Wauters, Ch Weinheimer, D. Zákoucký, and N. Severijns. Simbuca, using a graphics card to simulate Coulomb interactions in a penning trap. *Nucl. Instruments Methods Phys. Res. Sect. A Accel. Spectrometers, Detect. Assoc. Equip.*, 638(1):192–200, may 2011.
- [25] D. H.E. Dubin and T. M. O’Neil. Computer simulation of ion clouds in a penning trap. *Phys. Rev. Lett.*, 60(6):511–514, 1988.
- [26] S Sevugarajan and A.G. Menon. Frequency perturbation in nonlinear Paul traps. *Int. J. Mass Spectrom.*, 197(1-3):263–278, feb 2000.
- [27] Frank A. Londry, Roland L. Alfred, and Raymond E. March. Computer simulation of single-ion trajectories in paul-type ion traps. *J. Am. Soc. Mass Spectrom.*, 4(9):687–705, sep 1993.
- [28] Samuel Earnshaw. On the nature of the molecular forces which regulate the constitution of the luminiferous ether. *Trans. Cambridge Philos. Soc.*, 7:97, 1848.
- [29] Carolo Friderico Gauss. Theoria Attractionis Corporum Sphaeroidicorum Ellipticorum Homogeneorum. *Werke*, pages 3–22, 1877.
- [30] Robert Weinstock. On a fallacious proof of Earnshaw’s theorem. *Am. J. Phys.*, 44(4):392–393, apr 1976.

- [31] Lowell S. Brown and Gerald Gabrielse. Geonium theory: Physics of a single electron or ion in a Penning trap. *Rev. Mod. Phys.*, 58(1):233–311, jan 1986.
- [32] Katrin Kromer. *Environmentally-induced systematic effects at the high-precision mass spectrometer PENTATRAP*. Master thesis, Ruprecht Karl University of Heidelberg, 2019.
- [33] F. Herfurth K. Blaum. *Trapped Charged Particles and Fundamental Interactions*, volume 749 of *Lecture Notes in Physics*. Springer Berlin Heidelberg, Berlin, Heidelberg, 2008.
- [34] G. Bollen, R. B. Moore, G. Savard, and H. Stolzenberg. The accuracy of heavy-ion mass measurements using time of flight-ion cyclotron resonance in a Penning trap. *J. Appl. Phys.*, 68(9):4355–4374, nov 1990.
- [35] Martin Kretzschmar. Particle motion in a Penning trap. *Eur. J. Phys.*, 12(5):240–246, sep 1991.
- [36] Christian-Eric Roux. *High-resolution mass spectrometry: The trap design and detection system of Pentatrap and new Q-values for neutrino studies*. Doctoral thesis, Ruprecht Karl University of Heidelberg, 2012.
- [37] Florian Köhler-Langes. *The Electron Mass and Calcium Isotope Shifts*. Springer Theses. Springer International Publishing, Cham, 2017.
- [38] Jochen Ketter. *Theoretical treatment of miscellaneous frequency-shifts in Penning traps with classical perturbation theory*. Dissertation, Ruprecht Karl University of Heidelberg, 2015.
- [39] G. Gabrielse, L. Haarsma, and S.L. Rolston. Open-endcap Penning traps for high precision experiments. *Int. J. Mass Spectrom. Ion Process.*, 88(2-3):319–332, apr 1989.
- [40] Julia Maria Anne Repp. *The setup of the high-precision Penning- trap mass spectrometer PENTATRAP and first production studies of highly charged ions*. Dissertation, Ruprecht Karl University of Heidelberg, 2012.
- [41] Stefan Ulmer. *First Observation of Spin Flips with a Single Proton Stored in a Cryogenic Penning Trap*. PhD thesis, Ruprecht-Karls-Universität, Heidelberg, jul 2011.
- [42] J. Verdú, S. Kreim, K. Blaum, H. Kracke, W. Quint, S. Ulmer, and J. Walz. Calculation of electrostatic fields using quasi-Green’s functions: application to the hybrid Penning trap. *New J. Phys.*, 10(10):103009, oct 2008.

- [43] Jochen Ketter, Tommi Eronen, Martin Höcker, Sebastian Streubel, and Klaus Blaum. First-order perturbative calculation of the frequency-shifts caused by static cylindrically-symmetric electric and magnetic imperfections of a Penning trap. *Int. J. Mass Spectrom.*, 358(1):1–16, jan 2014.
- [44] Martin Kretzschmar. Theory of simultaneous dipole and quadrupole excitation of the ion motion in a Penning trap. *Int. J. Mass Spectrom.*, 325-327:30–44, jul 2012.
- [45] K. Blaum, G. Bollen, F. Herfurth, A. Kellerbauer, H-J Kluge, M. Kuckein, S. Heinz, P. Schmidt, and L. Schweikhard. Recent developments at ISOLTRAP: towards a relative mass accuracy of exotic nuclei below 10^{-8} . *J. Phys. B At. Mol. Opt. Phys.*, 36(5):921–930, mar 2003.
- [46] G. Bollen, R. B. Moore, G. Savard, and H. Stolzenberg. The accuracy of heavy-ion mass measurements using time of flight-ion cyclotron resonance in a Penning trap. *J. Appl. Phys.*, 68(9):4355–4374, nov 1990.
- [47] M. König, G. Bollen, H.-J. Kluge, T. Otto, and J. Szerypo. Quadrupole excitation of stored ion motion at the true cyclotron frequency. *Int. J. Mass Spectrom. Ion Process.*, 142(1-2):95–116, mar 1995.
- [48] Eric A Cornell, Robert M Weisskoff, Kevin R Boyce, and David E Pritchard. Mode coupling in a Penning trap: π pulses and a classical avoided crossing. *Phys. Rev. A*, 41(1):312–315, jan 1990.
- [49] John David Jackson. *Classical Electrodynamics*. John Wiley & Sons Inc, New Jersey, 3 edition, feb 1998.
- [50] Gouri Dhatt, Lefrançois Emmanuel, and Touzot Gilbert. *Finite Element Method*. Wiley, 1 edition, 2014.
- [51] Tarek I. Zohdi. *A Finite Element Primer for Beginners*. Springer International Publishing, Cham, dec 2018.
- [52] Roland Glowinski and Pekka Neittaanmäki, editors. *Partial Differential Equations*, volume 16 of *Computational Methods in Applied Sciences*. Springer Netherlands, Dordrecht, 2008.
- [53] Thomas Rylander, Par Ingelström, and Anders Bondeson. *Computational Electromagnetics*. Texts in Applied Mathematics. Springer New York, New York, NY, 2013.
- [54] Bin Zheng. Handbook of Medical Imaging. *Radiology*, 220(2):372–372, aug 2001.

- [55] Ian Goodfellow Courville, Yoshua Bengio, and Aaron. *Deep Learning*. MIT Press, 2016.
- [56] Ashish Sen and Muni Srivastava. *Regression Analysis*. Springer Texts in Statistics. Springer New York, New York, NY, 1990.
- [57] Graeme Hutcheson. Ordinary Least-Squares Regression. In *Multivar. Soc. Sci.*, pages 56–113. SAGE Publications, Ltd., 6 Bonhill Street, London EC2A 4PU, 2011.
- [58] Brian Bradie. *A Friendly Introduction to Numerical Analysis*. Pearson Education India, 2006.
- [59] David F. Griffiths and Desmond J. Higham. *Numerical Methods for Ordinary Differential Equations*. Springer Undergraduate Mathematics Series. Springer London, London, 2010.
- [60] Jay Boris and Ramy Shanny. Proceedings of the Fourth Conference on Numerical Simulation of Plasmas. page 3, Washington, D.C., 1970. Naval Research Laboratory.
- [61] T. Tajima. Plasma physics via computer simulation. *Comput. Phys. Commun.*, 42(1):151–152, sep 1986.
- [62] P. H. Stoltz, J. R. Cary, G. Penn, and J. Wurtele. Efficiency of a Boris-like integration scheme with spatial stepping. *Phys. Rev. Spec. Top. - Accel. Beams*, 5(9):094001, sep 2002.
- [63] G. Penn, P. H. Stoltz, J. R. Cary, and J. Wurtele. Boris push with spatial stepping. *J. Phys. G Nucl. Part. Phys.*, 29(8):1719–1722, aug 2003.
- [64] Hong Qin, Shuangxi Zhang, Jianyuan Xiao, Jian Liu, Yajuan Sun, and William M. Tang. Why is Boris algorithm so good? *Phys. Plasmas*, 20(8):084503, aug 2013.
- [65] Lubos Brieda. *Plasma Simulations by Example*. CRC Press, dec 2019.
- [66] O. Buneman. Time-reversible difference procedures. *J. Comput. Phys.*, 1(4):517–535, jun 1967.
- [67] David A. Dillard. *Advances in structural adhesive bonding*. Woodhead Publishing Limited, 2010.
- [68] Lars-Erik Lindgren. *Computational welding mechanics*. Woodhead Publishing Limited, 2007.
- [69] Charles R. Harris, K. Jarrod Millman, Stéfan J. van der Walt, Ralf Gommers, Pauli Virtanen, David Cournapeau, Eric Wieser, Julian Taylor, Sebastian Berg, Nathaniel J.

- Smith, Robert Kern, Matti Picus, Stephan Hoyer, Marten H. van Kerkwijk, Matthew Brett, Allan Haldane, Jaime Fernández del Río, Mark Wiebe, Pearu Peterson, Pierre Gérard-Marchant, Kevin Sheppard, Tyler Reddy, Warren Weckesser, Hameer Abbasi, Christoph Gohlke, and Travis E. Oliphant. Array programming with NumPy. *Nature*, 585(7825):357–362, sep 2020.
- [70] Nicholas J. Higham. *Accuracy and Stability of Numerical Algorithms*. Society for Industrial and Applied Mathematics, jan 2002.
- [71] Peter J. Rousseeuw and Christophe Croux. Alternatives to the Median Absolute Deviation. *J. Am. Stat. Assoc.*, 88(424):1273–1283, dec 1993.
- [72] Christophe Leys, Christophe Ley, Olivier Klein, Philippe Bernard, and Laurent Licata. Detecting outliers: Do not use standard deviation around the mean, use absolute deviation around the median. *J. Exp. Soc. Psychol.*, 49(4):764–766, jul 2013.
- [73] A. M. Stewart. Vector potential of the Coulomb gauge. *Eur. J. Phys.*, 24(5):519–524, sep 2003.
- [74] J. D. Jackson. From Lorenz to Coulomb and other explicit gauge transformations. *Am. J. Phys.*, 70(9):917–928, sep 2002.
- [75] BIPM. *Le Système international d’unités / The International System of Units (‘The SI Brochure’)*. Bureau international des poids et mesures, ninth edition, 2019.
- [76] L. Gastaldo, K. Blaum, K. Chrysalidis, T. Day Goodacre, A. Domula, M. Door, H. Dorrer, Ch E. Düllmann, K. Eberhardt, S. Eliseev, C. Enss, A. Faessler, P. Filianin, A. Fleischmann, D. Fonnesu, L. Gamer, R. Haas, C. Hassel, D. Hengstler, J. Jochum, K. Johnston, U. Keschull, S. Kempf, T. Kieck, U. Köster, S. Lahiri, M. Maiti, F. Mantegazzini, B. Marsh, P. Neroutsos, Yu N. Novikov, P. C. O. Ranitzsch, S. Rothe, A. Rischka, A. Saenz, O. Sander, F. Schneider, S. Scholl, R. X. Schüssler, Ch Schweiger, F. Simkovic, T. Stora, Z. Szücs, A. Türlér, M. Veinhard, M. Weber, M. Wegner, K. Wendt, and K. Zuber. The electron capture in 163Ho experiment – ECHo. *Eur. Phys. J. Spec. Top.*, 226(8):1623–1694, jun 2017.
- [77] C F Gauss. *Theoria Combinationis Observationum Erroribus Minimis Obnoxiae, Supplementum*. Göttingen, Germany, 1880.
- [78] C F Gauss. Nachlass: Theoria interpolationis methodo nova tractata. *Carl Friedrich Gauss, Werke*, 3:265–303, 1866.
- [79] Rainer Storn and Kenneth Price. Differential Evolution – A Simple and Efficient Heuristic for global Optimization over Continuous Spaces. *J. Glob. Optim.* 1997 114, 11(4):341–359, 1997.

- [80] Rainer Storn. On the usage of differential evolution for function optimization. In *Proc. North Am. Fuzzy Inf. Process.*, pages 519–523. IEEE, 1996.
- [81] Sven Sturm. *The g-factor of the electron bound in 28Si^{13+} : The most stringent test of bound-state quantum electrodynamics*. Phd thesis, Johannes-Gutenberg Universität, Mainz, 2012.
- [82] Molei Tao. Explicit high-order symplectic integrators for charged particles in general electromagnetic fields. *J. Comput. Phys.*, 327:245–251, dec 2016.
- [83] Molei Tao. Explicit symplectic approximation of nonseparable Hamiltonians: Algorithm and long time performance. *Phys. Rev. E*, 94(4):043303, oct 2016.

Acknowledgments

First and foremost, I would like to thank all the members of the Blaum Group for making me feel welcome in the group, for the pleasant working atmosphere, and for all friendly conversations, discussions and cooperation.

Special thanks to ...

Prof. Dr. Klaus Blaum for introducing me into his group and for our interesting discussions and talks.

PD Dr. Wolfgang Quint who kindly agreed and took the time to be the second reviewer of this thesis.

Dr. Sergey Eliseev for providing me with the opportunity to work in his group, for always having a friendly ear for my project and for our fruitful discussions.

Christoph Schweiger for being the supervisor of my project and for guiding me through this work.

Dr. Alexander Rischka for supporting this work through his theoretical and experimental experience.

Menno Door, Dr. Pavel Filianin, Jost Herkenhoff, Kathrin Kromer, Daniel Lange, and **Berkan Oskay** for your support and for proofreading this work.

Christian Will for bringing the topic of symplectic integration algorithms to my attention and for sharing his simulation knowledge.

Patricia Maria Vieten for supporting me in all aspects of life and for proofreading and discussing this work.

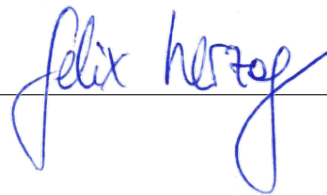
Last but not least, I would like to thank my parents for supporting me in my decision to study physics in Heidelberg.

Declaration / Erklärung

Except where stated otherwise by reference or acknowledgement, the work presented is entirely my own.

Ich versichere, dass ich diese Arbeit selbstständig verfasst und keine anderen als die angegebenen Quellen und Hilfsmittel benutzt habe.

Heidelberg, 23 March 2022



A handwritten signature in blue ink, reading "Felix Herzig", is written over a horizontal line.